HHS Public Access

Author manuscript

Cancer Cell. Author manuscript; available in PMC 2021 February 26.

Published in final edited form as:

Cancer Cell. 2017 June 12; 31(6): 771–789.e6. doi:10.1016/j.ccell.2017.05.006.

Kupffer Cell-Derived Tnf Triggers Cholangiocellular Tumorigenesis through JNK due to Chronic Mitochondrial Dysfunction and ROS

Detian Yuan[1,2], **Shan Huang**[2], **Emanuel Berger**[3], **Lei Liu**[4], **Nina Gross**[5], **Florian Heinzmann**[6,7], **Marc Ringelhan**[1,5], **Tracy O. Connor**[1,2], **Mira Stadler**[2], **Michael Meister**[2], **Julia Weber**[5], **Rupert Öllinger**[5], **Nicole Simonavicius**[1], **Florian Reisinger**[1], **Daniel Hartmann**[4], **Rüdiger Meyer**[8], **Maria Reich**[9], **Marco Seehawer**[6,7], **Valentina Leone**[1], **Bastian Höchst**[10], **Dirk Wohlleber**[10], **Simone Jörs**[5], **Marco Prinz**[11,12], **Duncan Spalding**[13], **Ulrike Protzer**[1], **Tom Luedde**[14], **Luigi Terracciano**[15], **Matthias Matter**[15], **Thomas Longerich**[16], **Percy Knolle**[10], **Thomas Ried**[8], **Verena Keitel**[9], **Fabian Geisler**[5], **Kristian Unger**[17], **Einat Cinnamon**[18], **Eli Pikarsky**[18,19], **Norbert Hüser**[4], **Roger J. Davis**[20], **Darjus F. Tschaharganeh**[21], **Roland Rad**[5], **Achim Weber**[22], **Lars Zender**[6,7,23], **Dirk Haller**[3,24,25,*], **Mathias Heikenwalder**[1,2,25,26,*]

[1]Institute of Virology, Technische Universität München and Helmholtz Zentrum München, 81675 Munich, Germany [2]Division of Chronic Inflammation and Cancer, German Cancer Research Center (DKFZ), 69120 Heidelberg, Germany [3]Chair of Nutrition and Immunology, Technische Universität München, Gregor-Mendel-Straße 2, 85350 Freising-Weihenstephan, Germany [4]Department of Surgery, Technische Universität München, 81675 Munich, Germany [5]2nd Department of Internal Medicine, Klinikum Rechts der Isar, Technische Universität München, 81675 Munich, Germany [6]Department of Internal Medicine VIII, University Hospital Tübingen, 72076 Tübingen, Germany [7]Department of Physiology I, Institute of Physiology, Eberhard Karls University Tubingen, 72076 Tübingen, Germany [8]Genome Technology Branch, National Human Genome Research Institute, U.S. National Institutes of Health, Bethesda, MD 20892, USA [9]Clinic for Gastroenterology, Hepatology, and Infectious Diseases, Heinrich-Heine University, 40204 Düsseldorf, Germany [10]Institute of Molecular Immunology, Klinikum rechts der Isar, Technische Universität München, 81675 Munich, Germany [11]Institute of Neuropathology, University of Freiburg, 79106 Freiburg, Germany [12]BIOSS Centre for Biological Signalling Studies, University of Freiburg, 79106 Freiburg, Germany [13]Department of Surgery and Cancer, Imperial College London, London SW7 2AZ, UK [14]Division of Gastroenterology, Hepatology and Hepatobiliary Oncology, RWTH Aachen University, 52074 Aachen, Germany [15]Institute of Pathology, University Hospital of Basel, 4003 Basel, Switzerland [16]Institute of Pathology, University Hospital RWTH,

[*]Correspondence: dirk.haller@tum.de (D.H.), m.heikenwaelder@dkfz-heidelberg.de (M.H.).

AUTHOR CONTRIBUTIONS

D.Y. and M.H. developed hypotheses, designed experiments, and wrote the manuscript. D.Y., M.H., and D.H. coordinated and supervised data analysis. D.Y., E.B., S.H., N.S., L.L., N.G., F.H., J.W., R.Ö., F.R., M.R., T.O.C., R.M., M. Stadler, M.M., M.R., M. Seehawer, V.L., B.H., D.W., and S.J. performed experiments. L.L., D.H., D.S., L.T., T. Longerich, N.H., and A.W. provided patient samples. M.P., U.P., M.M., L.T., T. Luedde, P.K., T.R., V.K., F.G., E.C., E.P., K.U., N.H., L.S., R.R., A.W., R.J.D., L.Z., D.F.T., D.H., and M.H. supervised the collaborative activities in their respective laboratories. All authors provided feedback on the manuscript.

SUPPLEMENTAL INFORMATION

Supplemental Information includes eight figures and one table and can be found with this article online at http://dx.doi.org/10.1016/j.ccell.2017.05.006.

52074 Aachen, Germany [17]Research Unit of Radiation Cytogenetics, Helmholtz Zentrum München, 85764 Neuherberg, Germany [18]The Lautenberg Center for Immunology and Cancer Research, IMRIC, Hebrew University-Hadassah Medical School, Jerusalem 91120, Israel [19]Department of Pathology, Hadassah-Hebrew University Medical Center, Jerusalem 91120, Israel [20]Howard Hughes Medical Institute and Program in Molecular Medicine, University of Massachusetts Medical School, Worcester, MA 01605, USA [21]Helmholtz-University Group “Cell Plasticity and Epigenetic Remodeling”, German Cancer Research Center (DKFZ) & Institute of Pathology University Hospital, 69120 Heidelberg, Germany [22]Department of Pathology and Molecular Pathology, University Zurich and University Hospital Zurich, 8091 Zurich, Switzerland [23]Translational Gastrointestinal Oncology Group within the German Consortium for Translational Cancer Research (DKTK), German Cancer Research Center (DKFZ), 69120 Heidelberg, Germany [24]ZIEL – Institute for Food & Health, Technische Universität München, 85350 Freising-Weihenstephan, Germany [25]These authors contributed equally [26]Lead Contact

SUMMARY

Intrahepatic cholangiocarcinoma (ICC) is a highly malignant, heterogeneous cancer with poor treatment options. We found that mitochondrial dysfunction and oxidative stress trigger a niche favoring cholangiocellular overgrowth and tumorigenesis. Liver damage, reactive oxygen species (ROS) and paracrine tumor necrosis factor (Tnf) from Kupffer cells caused JNK-mediated cholangiocellular proliferation and oncogenic transformation. Anti-oxidant treatment, Kupffer cell depletion, *Tnfr1* deletion, or JNK inhibition reduced cholangiocellular pre-neoplastic lesions. Liver-specific JNK1/2 deletion led to tumor reduction and enhanced survival in Akt/Notch- or p53/Kras-induced ICC models. In human ICC, high Tnf expression near ICC lesions, cholangiocellular JNK-phosphorylation, and ROS accumulation in surrounding hepatocytes are present. Thus, Kupffer cell-derived Tnf favors cholangiocellular proliferation/differentiation and carcinogenesis. Targeting the ROS/Tnf/JNK axis may provide opportunities for ICC therapy.

Graphical Abstract

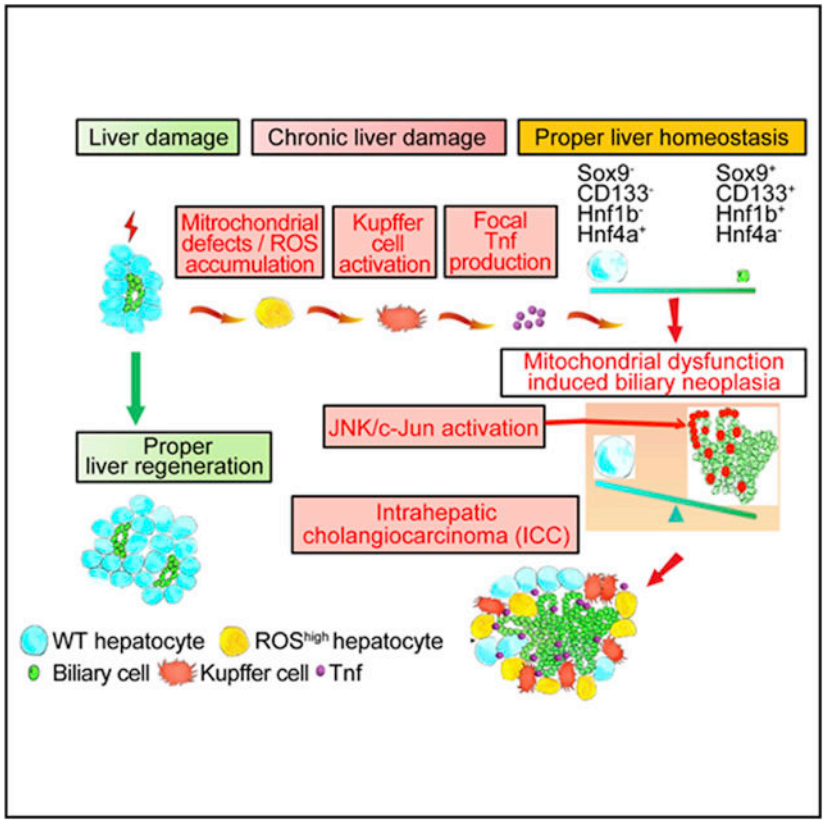

In Brief

Yuan et al. show that mitochondrial dysfunction and oxidative stress in the liver increase tumor necrosis factor (TNF) expression by Kupffer cells to cause JNK-mediated cholangiocellular proliferation and transformation. The ROS/TNF/JNK axis may be an effective target for intrahepatic cholangiocarcinoma therapy.

INTRODUCTION

Intrahepatic cholangiocarcinoma (ICC) is a liver cancer typically diagnosed at advanced stages, with poor prognosis and increasing incidence (Gatto and Alvaro, 2010). Cellular origins and molecular mechanisms underlying ICC progression are poorly understood (Zender et al., 2013; Zhang et al., 2008). ICC is observed in both diseases affecting biliary epithelial cells such as primary sclerosing cholangitis (Rizvi et al., 2015) and in diseases that cause chronic hepatocyte injury, such as chronic hepatitis C or B virus infection, chronic alcohol abuse, and nonalcoholic steatohepatitis (NASH) (Ariizumi and Yamamoto, 2014; Tyson and El-Serag, 2011). Of note, a common feature of these etiologies is mitochondrial dysfunction and high reactive oxygen species (ROS) levels.

Genomic and transcriptomic analyses revealed different mutational and transcriptome profiles between hepatocellular carcinoma (HCC) and ICC (Fujimoto et al., 2015; Jiao et al., 2013; Zou et al., 2014). A series of distinct developmental signals preferentially used by hepatocytes or cholangiocytes have been uncovered using rodent liver injury models

(Boulter et al., 2012; Kang et al., 2012). However, the role of pro-inflammatory signaling pathways in ICC development under conditions of chronic liver damage remains elusive. Excessive remodeling of the inflammatory microenvironment is known to occur in chronic liver disease (Szabo and Petrasek, 2015). Given recent studies indicating a link between pro-inflammatory signaling pathways and cell plasticity in the intestine and breast epithelium (Scheeren et al., 2014; Taniguchi et al., 2015), it is likely that such pathways, in addition to their roles in immune regulation, may shape the cell plasticity of liver cells.

The pro-inflammatory cytokine tumor necrosis factor (Tnf) is mainly secreted by Kupffer cells in adult livers (Roberts et al., 2007), and has pro-survival/pro-growth effects on cells of specific lineages during development (Espin-Palazon et al., 2014; Liu et al., 2014). Malignant cells may hijack the Tnf-dependent pro-survival program to obtain a selective growth advantage. Indeed, Tnf has been implicated in cancer progression by sustaining expansion of neoplastic cells, including skin cancer, cervical carcinomas, and HCC (Arnott et al., 2004; Nakagawa et al., 2014; Pikarsky et al., 2004; Woodworth et al., 1995). However, the effects of persistent Tnf production on cholangiocytes under conditions of chronic liver injury and high ROS have remained elusive.

Thus, in this study we examined the role of mitochondrial dysfunction and ROS in ICC development.

RESULTS

Hepatic Mitochondrial Dysfunction Leads to Severe Liver Damage, Hepatocyte Proliferation, and Premalignant Cholangiocellular Lesions

To determine the effect of high ROS and mitochondrial dysfunction on ICC development, we analyzed ICC mouse models, including CRISPR/Cas9-induced ICC (Weber et al., 2015), constitutively active Akt-1 (Akt), together with Nras- (Akt/Nras) or Notch1-induced ICC (Akt/Notch) (Matter et al., 2016), and transposon-mediated in vivo delivery of KrasG12D-induced ICC (HDTV Kras) (M.S. and L.Z., unpublished data). 8-Hydroxy-2-deoxyguanosine (8-OHdG), an indicator of secondary metabolites due to oxidative DNA damage, was evaluated in tumors and adjacent tissues. All four ICC models exhibited extensive 8-OHdG staining in $CK19^{+}$ neoplastic cells compared with normal cholangiocytes. Intriguingly, 8-OHdG positivity was not only seen in malignant cholangiocytes, but also in surrounding hepatocytes (Figure S1A), implying that oxidative stress in the liver microenvironment could correlate with ICC development.

We next performed 8-OHdG immunohistochemistry (IHC) in 121 human ICC samples. Nearly 80% of ICCs showed 8-OHdG^{+} malignant cholangiocytes as well as surrounding hepatocytes (Figure S1B), suggesting an association between oxidative stress and ICC development.

To mimic hepatic mitochondrial dysfunction, we generated knockin mice with *loxP* sites flanking exons 4 to 8 of *Hspd1* (Figure S1C) (Berger et al., 2016) and crossed them with Alb-Cre transgenics (Postic et al., 1999) to produce mice with liver-specific *Hspd1* deletion ($Hspd1^{\Delta LPC}$) (Figures S1D and S1E). qRT-PCR and Western blot revealed loss of Hspd1

transcript and protein in livers from 6-week-old mice (Figure S1F). IHC confirmed absence of Hspd1 in both hepatocytes and cholangiocytes (Figure S1G). Hepatic *Hspd1* deletion induced severe mitochondrial defects. Ultrastructural analyses revealed fragmented, enlarged and swollen mitochondria, and mitochondria encapsulated in double-membrane autophagosomes or autolysosomes (mitophagy) in Hspd1$^{\Delta LPC}$ livers (Figure 1A). Strong 8-OHdG staining in Hspd1$^{\Delta LPC}$ liver cells and elevated levels of oxidized protein by oxyblot analysis further confirmed ROS accumulation (Figures 1A and S1H).

Postnatal day 2 (P2) and day 7 (P7) Hspd1$^{\Delta LPC}$ livers showed no obvious histological or micro-architectural differences, excluding embryonic developmental defects (Figures S1I and S1J, data not shown). From the age of 4 to 6 weeks, Hspd1$^{\Delta LPC}$ mice exhibited weakness and weight loss and had to be euthanized due to severe weight loss at 8–9 weeks of age (Figures 1B, 1C, and S1K). Macroscopic signs of focal fibrosis and necrosis were evident as early as P38 in Hspd1$^{\Delta LPC}$ livers (Figure S1L). At 8 weeks, Hspd1$^{\Delta LPC}$ mice had significantly higher liver-to-body weight ratio, pale livers, and yellow-colored serum, indicative of cholestasis (Figures 1D–1F and S1M). Serum analyses showed a progressive increase of ALT, AST, AP, and bilirubin levels over time (Figure S1N), indicating hepatocyte and bile duct damage. H&E and TUNEL staining revealed widespread hepatocyte cell death (Figure S1O), not attributable to caspase-3 activation (Figure S1P). Sirius Red staining at 8 weeks revealed severely altered liver architecture with concomitant collapse, regeneration, and fibrosis (Figure S1Q). Hepatocyte death and bile duct defects coincided with disturbed liver functions (Figure S1R). All of the above-described pathologic manifestations point to severe liver damage suggestive of liver failure, which most likely accounts for the premature lethality of the Hspd1$^{\Delta LPC}$ mice.

Focal areas of hepato- and cholangiocellular regeneration were found from 6 weeks onwards (Figures 1G and 1H), accompanied by upregulation of Sox9, cell-cycle-related proteins Pcna and Cyclin D1, and p-Akt (Figures S1S and S1T). Ki67^{+} hepatocytes forming regenerative nodules were Hspd1^{+} (Figure S1U), while Hspd1^{-} hepatocytes were rarely Ki67^{+} in 8-week-old Hspd1$^{\Delta LPC}$ livers (Figure S1V). PCR and qRT-PCR of regenerative nodules and surrounding Hspd1^{-} hepatocytes revealed that the *Hspd1*$^{loxP/loxP}$ alleles were largely intact in regenerative hepatocytes, in contrast to surrounding Hspd1^{-} regions (Figures S1W and S1X). Next, we crossed Hspd1$^{\Delta LPC}$ mice with the stochastic multicolor Cre-recombinase reporter line, Confetti (Livet et al., 2007). Hspd1^{-} hepatocytes were labeled with multi-colored fluorescent proteins, while Hspd1^{+} hepatocytes remained unlabeled in 8-week-old Hspd1$^{\Delta LPC}$ mice, supporting the lack of Cre-mediated recombination in regenerating Hspd1^{+} hepatoctyes (Figure S2A).

In parallel with proliferating hepatocytes, marked expansion of cholangiocytes was observed, including glands or trabecular structures of cells with scant cytoplasm and hyperchromatic nuclei by 7–8 weeks (Figures 1F, 1G, S2B, and S2C). Cholangiocellular lesions, characterized by irregular glands, loss of polarity, multi-layering of cells, and frequent mitosis, were evident in 8-week-old Hspd1$^{\Delta LPC}$ livers (Figure 1H). These foci, assessed by board-certified pathologists, resembled human biliary intraepithelial neoplasia, a precursor cancerous ICC lesion (Rougemont et al., 2010). Cholangiocellular lesions were positive for pan-CK, A6, CK19, and Erbb2, and negative for α-fetoprotein (Afp) and

intestinal lineage markers, underlining the biliary fate of these cells (Figures S2D–S2F). Furthermore, these lesions co-stained for validated cancer stem cell (CSC) markers CD44v6 and CD90.1, c-Myc, and for collagen IV-positive stromal reaction as seen in human ICC (Figures 1I and S2D). Microarray-based comparative genomic hybridization analysis of laser-dissected $CK19^+$ cholangiocellular lesions from independent $Hspd1^{\Delta LPC}$ livers revealed copy-number changes of >9% across the genome compared with controls (Figure 1J). Synteny analyses revealed that 95% of chromosomal losses and 53% of chromosomal gains in $Hspd1^{\Delta LPC}$ livers were congruent with loci in the human cholangiocarcinoma cohort from The Cancer Genome Atlas ($p < 0.0001$, Fisher's exact test) (Figure S2G). Transplantation of liver pieces from one out of three 8-week-old $Hspd1^{\Delta LPC}$ donor mice resulted in tumor formation with ICC, but not HCC characteristics, including glandular structures and $CK19^+$ cells in three out of four transplantation experiments in severe combined immunodeficiency Beige recipient mice (Figures 1K and S2H), supporting their malignant potential. Comparable cholangiocellular lesions were absent in several other liver injury models investigated (Figure S2I). Similar to regenerating hepatocytes, proliferating cholangiocytes were almost exclusively $Hspd1^+$ (Figures 1F and S2J). Tracing with Confetti-$Hspd1^{\Delta LPC}$ mice further showed lack of Cre-recombinase activity in these cells (Figure S2K).

Using an adeno-associated virus (AAV) vector Cre expression system (Figure S2L) (Malato et al., 2011), we reproduced this phenotype in *Hspd1*$^{loxP/loxP}$ mice. Progressive postnatal deletion of *Hspd1* was restricted to hepatocytes from 2 weeks post-AAV8 injection on (AAV8-Cre *Hspd1*$^{loxP/loxP}$) (Figure S2M), including progressive liver damage, cholestasis, and cholangiocellular proliferation at 6–8 weeks post injection (Figures 1L, 1M, S2N, and S2O). Hspd1 expression in these cholangiocellular lesions was observed by IHC (Figure S2P). This confirms the non-cell-autonomous mode of ICC development upon Hspd1 deficiency, and suggests that the phenotype does not result from developmental defects due to Cre induction.

Mitochondrial Dysfunction Induces an Oxidative and Pro-carcinogenic Environment in $Hspd1^{\Delta LPC}$ Livers

Genes involved in mitochondria homeostasis, the mitochondrial respiratory chain, and molecules downstream of CHOP (encoded by *Ddit3*) capable of regulating cell death were upregulated in $Hspd1^{\Delta LPC}$ livers (Figures S3A and S3B). In contrast, most ER unfolded protein response associated genes remained unchanged, indicating that mitochondrial UPR (mtUPR) is primarily responsive to Hspd1 deficiency. A large panel of anti-oxidant enzymes was also strongly upregulated in Hspd1-deficient livers (Figures 2A and S3C). 8-OHdG extensively labeled $Hspd1^-$ but not $Hspd1^+$ hepatocytes (Figure 2B). Early increase of phosphorylated Eif2a (p-Eif2a) and CHOP was confirmed in $Hspd1^{\Delta LPC}$ livers from 4 weeks by Western blot (Figure 2C). Increased phosphatidylethanolamine-conjugated LC3 (LC3-II) was also observed, providing ultrastructural evidence of mitophagy in $Hspd1^{\Delta LPC}$ hepatocytes (Figures 1A and 2C).

We next investigated which signaling pathways were activated downstream of ROS: phosphorylation of JNK and Erk1/2, along with HCC markers, were elevated in $Hspd1^{\Delta LPC}$

livers from week 4 (Figure 2D) but not p-p38 MAPK (Figure S3D). Staining consecutive sections revealed that most p-JNK^{+} cells were Hspd1^{-} (Figure S3E). JNK activation was corroborated by nuclear translocation of c-Jun (Figure S3E). Screening also identified c-Myc, Kras, and Src as the top upregulated pro-survival genes in Hspd1$^{\Delta LPC}$ livers (Figures 2D, 2E, and S3F), the expression of which was mainly restricted to Hspd1^{-} areas by IHC (Figures 2F and S3G–S3I). Thus, mitochondrial defects driven by Hspd1 loss may induce an oxidative and pro-survival/oncogenic microenvironment stimulating growth of surrounding wild-type (WT) cells.

Anti-oxidant BHA Attenuates ROS Accumulation and Formation of Premalignant Cholangiocellular Lesions

To examine the role of ROS in Hspd1$^{\Delta LPC}$ liver pathology, Hspd1$^{\Delta LPC}$ mice were fed chow containing the anti-oxidant butylated hydroxyanisole (BHA) starting at the age of 4 weeks. BHA reduced 8-OHdG staining, expression of ROS-scavenging enzymes, and Afp level in Hspd1$^{\Delta LPC}$ livers (Figures S4A and S4B), indicating efficient ROS blockade. Remarkably, treating Hspd1$^{\Delta LPC}$ mice with BHA strongly attenuated macroscopically visible liver damage, weight loss, and prevented early lethality (Figures 3A, 3B, and S4C). At 8 weeks, hepatocyte necrosis and serum liver enzymes were significantly reduced (Figures 3C, 3D, and S4D). Intriguingly, BHA almost completely blocked cholangiocyte proliferation and development of cholangiocellular lesions (Figures 3E and S4E). In contrast, no effect on hepatocyte proliferation or cyclin D1 expression was found (Figure S4F). Accordingly, CK19 expression was suppressed and hepatocyte nuclear factor 4α (*Hnf4a*) and *Aldh2* levels were partially rescued at 8 weeks (Figures 3F and S4G). Compensatory proliferation of WT hepatocytes reversed weight loss in Hspd1$^{\Delta LPC}$ mice around weeks 18 to 20 (Figures S4C and S4H).

Analysis of downstream signaling revealed that p-JNK was dampened by BHA (Figures 3G and 3H), while Erk1/2, p38 MAPK, and Eif2a were unaffected (Figures 3G, 3H, and S4I). Moreover, BHA normalized expression of pro-survival genes (Figures 3G, 3J, and S4G). However, CHOP expression was further elevated by BHA (Figures 3G and 3I). This was possibly due to BHA itself, as BHA-fed WT mice also had elevated CHOP (Figures 3G and S4J). BHA did not attenuate *Hspa9*, p-Eif2a, or LC3-II (Figures 3J and S4I). Thus, anti-oxidant treatment appeared to protect Hspd1$^{\Delta LPC}$ mice by inhibiting ROS and its downstream pro-carcinogenic signaling pathways rather than attenuating mtUPR signaling (Figure 3K).

Kupffer Cell-Derived Tnf Promotes Premalignant Cholangiocellular Lesions

Next, we investigated the propagating factors that link high ROS levels and the pro-carcinogenic niche with the neoplastic phenotype. We measured mRNA expression of cytokines/ligands in Hspd1$^{\Delta LPC}$ and WT livers (Figure 4A). Strikingly, rapid and robust induction of *Tnf* mRNA and protein levels, far exceeding other candidates, was observed (Figures 4A, 4B, and S5A). By contrast, *Il6* mRNA levels were not changed and even reduced at protein level (Figures 4A and S5A), suggesting a niche favoring cholangiocellular proliferation. Consistent with the ameliorated Hspd1$^{\Delta LPC}$ phenotype, Tnf expression was strongly attenuated upon BHA treatment (Figures 4B and 4C).

Cells under stress conditions release pro-inflammatory cytokines into the environment as "endogenous danger signals" (Shi et al., 2003). Indeed, cytokines known to activate Kupffer cells, including Ccl2, Ccl5, and interleukin 1β (IL-1β), were upregulated in Hspd1$^{\Delta LPC}$ livers and reduced by BHA treatment (Figure S5B). IHC and in situ hybridization revealed that focal Tnf expression mainly localized to F4/80^{+} Kupffer cells (Figures 4D and S5C), the numbers of which were more extensively increased in Hspd1$^{\Delta LPC}$ livers compared with T and B lymphocytes and neutrophils (Figure S5D). qRT-PCR analysis of *Tnf* mRNA in purified liver cells confirmed that Tnf is mainly produced by Kupffer cells (Figure S5E). Treating primary Kupffer cells or a murine myeloid cell line (RAW 264.7) with supernatant of primary hepatocytes isolated from Hspd1$^{\Delta LPC}$ mice or H_2O_2-treated primary WT hepatocytes increased *Tnf* expression (Figure S5F). *Tnf* expression was inhibited by the inflammasome inhibitor isoliquiritigenin (Huang et al., 2013), but not by inhibitors of several other pathways (Figure S5G). In addition, less activated Kupffer cells in BHA-treated Hspd1$^{\Delta LPC}$ mice correlated with attenuated Tnf expression (Figures 4B, 4C, and S5H). Furthermore, immunofluorescence and in situ hybridization for Tnfr1 showed enriched expression in biliary epithelial cells and cholangiocellular lesions when compared with surrounding hepatocytes (Figures 4E, 4F, and S5I). Therefore, Tnf from Kupffer cells could link ROS production to cholangiocellular tumorigenesis in Hspd1$^{\Delta LPC}$ mice.

Next, we depleted Kupffer cells by liposomal clodronate injection in Hspd1$^{\Delta LPC}$ mice once every 3 days from weeks 6 to 8 (Figure 4G). One day after the final injection, depletion efficacy in liver and spleen was confirmed by F4/80 IHC (Figures 4H and S5J). Clodronate significantly reduced Tnf levels in Hspd1$^{\Delta LPC}$ livers (Figure 4I), and cholangiocyte proliferation and development of cholangiocellular lesions were almost entirely abolished (Figures 4H and S5K), while Ki67^{+} hepatocytes increased up to 1.84-fold (Figures 4J and S5L). Clodronate-treated Hspd1$^{\Delta LPC}$ mice began to restore body weight from day 42 (Figure S5M), and 8-week-old mice had rescued liver architecture and decreased liver enzymes (Figures S5N and S5O). Clodronate-treated Hspd1$^{\Delta LPC}$ mice displayed no abnormalities up to 4 months (Figure S5N), indicating that cholangiocellular overgrowth in Hspd1$^{\Delta LPC}$ mice is triggered by Tnf from Kupffer cells in response to hepatic mitochondrial dysfunction and oxidative stress.

Tnfr1 Signaling Promotes Formation of Premalignant Cholangiocellular Lesions

Next, we treated primary cholangiocytes isolated from WT or *Tnfr1*$^{-/-}$ mice with Tnf. After 5 days, WT cholangiocytes showed a 2.5-fold increase in bromodeoxyuridine incorporation, which was comparable with the mitogenic effect of Egf together with forskolin (Figure 5A). Tnfr1 deficiency altered the response of cholangiocytes to Tnf, but not to Egf and forskolin (Figure 5A), confirming that the mitogenic effect of Tnf is mediated by Tnfr1. We then tested the effect of Tnf on bipotential hepatoblasts isolated from E14.5 livers (Nitou et al., 2002). To induce differentiation, hepatoblasts were maintained in basal medium with DMSO for 7 days. Biliary lineage markers A6 and CK19 were downregulated, while hepatocyte lineage markers Hnf4α and Afp were highly expressed (Figures 5B and S5P). Strikingly, when hepatoblasts were treated with Tnf, cells adopted a biliary morphology (Figures 5B and S5P). IHC indicated high A6 and strongly reduced Hnf4α expression, suggesting that Tnf can bias toward a cholangiocellular cell fate in hepatoblasts (Figures 5B and S5P).

These data were also reproduced in bipotential HepaRG cells (Figure S5Q), strongly suggesting that Tnf can promote cholangiocellular differentiation and proliferation of bipotential hepatic cells in vitro.

Next, we generated Hspd1$^{\Delta LPC}$ *Tnfr1*$^{-/-}$ double knockout mice. Loss of Tnfr1 in Hspd1$^{\Delta LPC}$ mice prevented early lethality and significantly reduced liver damage at 8 weeks (Figures 5C, 5D, S5R, and S5S). Interestingly, while in most Hspd1$^{\Delta LPC}$ *Tnfr1*$^{+/-}$ mice lethality was prevented, 4 out of 18 were not, indicating the dose dependence of Tnfr1 (Figures 5C and S5S). Importantly, the prevention of cholangiocellular overgrowth was unlikely to be dependent on the pro-survival or pro-apoptotic function of Tnfr1: equal levels of necrosis were observed in Hspd1$^{\Delta LPC}$ as well as in 6-week-old double knockout mice (Figures 5E and 5F). Likewise, ROS accumulation, as well as the resulting induction of *Gpx3*, Kupffer cell activation, and *Tnf* mRNA levels remained unchanged in Hspd1$^{\Delta LPC}$ *Tnfr1*$^{-/-}$ when compared with Hspd1$^{\Delta LPC}$ mice, suggesting that Kupffer cell activation and Tnf production were not affected by *Tnfr1* deletion (Figures 5G, 5H, and S5T). No difference in liver enzyme levels between Hspd1$^{\Delta LPC}$ *Tnfr1*$^{-/-}$ and Hspd1$^{\Delta LPC}$ mice was found by week 6 but ALT, AST, AP, and bilirubin were significantly reduced in double knockout mice by week 8 (Figure S5U). Consistent with the idea that Tnf promotes biliary proliferation, cholangiocellular overgrowth and CSC expansion was apparently blocked (Figures 5E–5H and S5V). Importantly, Ki67^{+} hepatocytes increased significantly in 8-week-old livers in double knockout mice at the expense of cholangiocytes (Figures 5E and 5I). One-year-old double knockout mice did not show any abnormalities (Figure S5W). Thus, Tnfr1 signaling favors biliary proliferation and neoplasia over hepatocyte proliferation under the conditions of mitochondrial dysfunction, ROS, and liver damage.

JNK/c-Jun Activation Is Required for Cholangiocellular Hyperproliferation

Tnf/Tnfr1 signaling activates a diverse set of downstream molecules, including Rela, Stat3, and JNK. We observed strong nuclear p-JNK staining in cholangiocytes, whereas nuclear Rela and Stat3 were mainly present in non-parenchymal cells (Figure 6A). Nuclear c-Jun was also observed in cholangiocytes of Hspd1$^{\Delta LPC}$ livers (Figure S6A). Similarly, primary hepatoblasts cultured with Tnf showed nuclear staining of c-Jun but not Rela (Figure 6B). Notably, nuclear p-JNK was specifically attenuated in cholangiocytes but not in hepatocytes after in vivo clodronate treatment (Figure S6B), indicating that JNK is activated downstream of Tnf.

To test the therapeutic potential of JNK inhibition on cholangiocellular overgrowth, the JNK inhibitor SP600125 was administered intraperitoneally (i.p.) daily for 2 weeks beginning at P36 in Hspd1$^{\Delta LPC}$ mice (Figure 6C). JNK inhibition reduced cholangiocellular lesions, resulting in proper regeneration and eventually functional livers with WT hepatocytes at week 16 (Figures 6D, S6C, and S6D). Cholangiocellular proliferation was also strongly reduced (Figure 6D), whereas hepatocyte proliferation was not influenced (Figure S6E). Since p-JNK was also found in Hspd1^{-} hepatocytes in untreated Hspd1$^{\Delta LPC}$ mice, SP600125 might also exert its role by attenuating hepatocyte injury and/or the carcinogenic signals in Hspd1^{-} hepatocytes. Indeed, we observed decreased nuclear p-JNK in both hepatocytes and cholangiocytes due to SP600125 treatment, accompanied by reduced

necrosis and liver enzymes and abolished c-Myc upregulation (Figures S6F–S6I). Expression of UPR-related and redox signaling-related genes also declined in livers of SP600125-treated Hspd1$^{\Delta LPC}$ mice, concomitant with reduced 8-OHdG staining (Figures S6J and S6K). In addition, less F4/80^{+} staining and lower levels of *Tnf* mRNA were evident (Figures S6J and S6K), indicating that Kupffer cell activation and Tnf production was attenuated. In contrast, Kupffer cell depletion strongly reduced p-JNK in cholangiocytes but not surrounding hepatocytes (Figure S6B), suggesting that JNK activation in cholangiocytes was dependent on paracrine Tnf.

To directly assess the role of JNK on biliary proliferation, isolated cholangiocytes were cultured with SP600125 in the presence of Tnf. Tnf-enhanced proliferation of WT cholangiocytes was abrogated by SP600125 treatment (Figure 5A). This result was confirmed with two additional JNK inhibitors (JNK-IN-8 and JNK6o; Figure S6L).

Hepatoblasts were also treated with SP600125 during in vitro differentiation. SP600125-treated hepatoblasts lacked c-Jun activation (Figures 6E and S6M). As a result, biliary differentiation of hepatoblasts was suppressed, with reduced ductular morphogenesis and decreased expression of A6 and CK19 (Figures 6F and 6G). Meanwhile, SP600125 treatment restored expression of hepatocyte markers Hnf4α and Afp comparable with controls (Figures 6F, 6G, and S6M). Therefore, JNK/c-Jun signaling appears to be activated by Tnf and required for biliary differentiation and proliferation.

The Tnf/JNK Signaling Axis Is Activated in Distinct Mouse ICC Models

Since both HCCs and ICCs were found in the multiplexed CRISPR/Cas9-induced liver cancer model (Weber et al., 2015), we were able to directly compare the molecular traits of HCC versus ICC. IHC revealed that JNK activation, Tnfr1 expression, and high levels of CK19 and Sox9 were exclusively present in ICC, but not in HCC or unaffected tissue (Figure 7A and S7A–S7C). Kupffer cell activation and Tnf production were strongly enriched in ICC samples, surrounding the malignant cholangiocytes, regardless of their distinct genetic signature (Figures 7B and S7D–S7F). Moreover, nuclear p-JNK was strongly enriched in all ICC models examined (Figures 7A and S7G), but absent from HCC models induced by chronic inflammation (Haybaeck et al., 2009) or NASH (Wolf et al., 2014) (Figure S7H).

JNK inhibition was tested on two aggressive ICC models by hydrodynamic tail vein injection of different sets of constructs (Akt/Notch; p53/Kras) into WT or liver-specific JNK1/2 knockout mice (JNK1/2$^{\Delta LPC}$). JNK1/2 knockout in liver parenchymal cells provided a strong survival benefit (e.g., >40 days in Akt/Notch; >25 days in p53/Kras) and significantly reduced tumor incidence in both models (Figures 7C–7F). IHC showed lack or reduction of tumors (Figure 7G). Tumors in JNK1/2$^{\Delta LPC}$ mice found at later time points displayed features of ICC (Figure S7I), suggesting the existence of uncharacterized JNK bypass signaling.

Next, we established an ICC cell line (mICC), derived from a multiplexed CRISPR/Cas9 ICC. mICC cells had reduced p-JNK and severe growth defects in the presence of SP600125 (Figures S7J and S7K). mICC cells were subcutaneously injected into mice, resulting in A6^{+}

and p-JNK$^+$ tumors with histological features similar to primary tumors of human ICC patients (Figure S7L). SP600125 was administered i.p. daily starting at day 1 post-inoculation for 7 days, which resulted in significantly reduced tumor formation (Figure S7M).

p-JNK is Strongly Increased in ICC Patient Specimens and Cell Lines

Next, we analyzed human HCC and ICC for Tnf and p-JNK by IHC (Figures 8A and S8A). Only 3.2% of HCC were Tnf$^+$, as opposed to 55.2% of ICC (Figure 8B). p-JNK was found in approximately 20% of HCC, as opposed to 80% in ICC (Figure 8C). We also found 8-OHdG$^+$ ICC predominantly surrounding hepatocytes but not in malignant cholangiocytes (Figure 8A), supporting our notion that mitochondrial dysfunction and oxidative stress can also drive JNK activation non-automatously.

Finally, we tested the response of well-characterized human ICC (ETK-1 and HuCCT-1) and HCC (Huh-7 and HepG2) cell lines to JNK inhibition. ICC cells had much higher p-JNK than HCC cells, consistent with our histopathological studies (Figure S8B). Inhibiting JNK activity impaired cell proliferation in a dose-dependent manner (Figures S8C–S8E). Both human ICC cell lines showed a higher sensitivity to SP600125 compared with HCC cell lines ($p < 0.001$, Figures S8D and S8E). ICC cell lines also showed a higher degree to which maximal growth inhibition was achieved by JNK inhibition (Figure S8E). Similar effects were seen with additional JNK inhibitors ($p < 0.01$, Figures S8F and S8G). This suggests that targeted inhibition of JNK signaling in ICC may have therapeutic value.

DISCUSSION

Mitochondrial dysfunction and ROS are common features of liver diseases (Kamata et al., 2005; Maeda et al., 2005; Szabo and Petrasek, 2015). A recent genetic screen in *Drosophila* indicated that mitochondrial defects and ROS activate oncogenic signaling in neighboring cells by forming a tumorigenic niche (Ohsawa et al., 2012). Here, we demonstrate that mitochondrial defects in hepatocytes trigger ROS accumulation leading to focal recruitment of Tnf-producing Kupffer cells, which create a favorable niche for biliary proliferation via JNK signaling. This suggests that the liver microenvironment could be pharmacologically manipulated to improve liver function in advanced liver disease.

Tnf/JNK/c-Jun signaling appears to induce a biliary proliferation program in hepatocytes or liver bipotential cells (Nishikawa et al., 2013), implicating this pathway in the pathogenesis of human cholangiocellular tumors. Examination of human specimens showed that Tnf and p-JNK were found far more frequently in ICC than in HCC, consistent with findings from others, showing that p-c-Jun emanates from infiltrating inflammatory cells in human HCC (Hefetz-Sela et al., 2014). Chemotherapeutic options for ICC are lacking due to unidentified ICC-specific targets. Our results with human HCC and ICC reveal distinct molecular traits of these two pathological entities, indicating that HCC and ICC may respond differently to the same treatment. Accordingly, cancer cells isolated from human ICC are more sensitive to JNK inhibition compared with cells from HCC. Further investigation of the link between p-JNK level and clinicopathological features may provide important clues regarding disease mechanisms.

Conflicting roles for Kupffer cells in hepatocyte regeneration, cholangiocellular growth (Boulter et al., 2012, 2015), and HCC development (Maeda et al., 2005; Zhu et al., 2000) have been reported. The role of Kupffer cells likely depends on the type of tissue injury. Indeed, the cytokine signatures of Kupffer cells isolated from CDE or DDC diet models are different (Boulter et al., 2012). In addition, the spatial regulation of the regenerative niche also differs in distinct contexts. In DDC-induced biliary regeneration, Kupffer cells are separated from ductular reactive cells (Boulter et al., 2012), whereas in Hspd1$^{\Delta LPC}$ and multiplexed CRISPR/Cas9 mice, Kupffer cells closely associate with cholangiocellular tumor cells. Thus, immune components appear to be highly adaptable to various stimuli. In addition, it remains to be determined how the crosstalk between Tnf and other signaling pathways (e.g., Wnt, Tgfb, Notch, and Hippo signaling) coordinates liver cell plasticity in different models of murine liver cancer (Boulter et al., 2015; Yimlamai et al., 2014; Zender et al., 2013).

Our analysis on human HCC and ICC revealed that a subgroup of HCC are strongly p-JNK^{+}. p-JNK/p-c-Jun positivity in HCC varies greatly across studies, from 11% (Hefetz-Sela et al., 2014) to 56% (Hui et al., 2008), probably due to sample heterogeneity. JNK activation has also been implicated in HCC development in mouse models. For instance, liver-specific *Mapk14* deletion leads to JNK hyperactivation and HCC development in diethylnitrosamine (DEN)-treated mice (Hui et al., 2007). JNK1-deficient mice show impaired HCC formation in a DEN-phenobarbital-induced mouse liver cancer model (Hui et al., 2008). JNK1 disruption also reverses increased susceptibility to DEN-induced HCC formation in Ikkb$^{\Delta Hep}$ mice (Sakurai et al., 2006). However, lack of JNK1 plus JNK2 in hepatocytes increases tumor burden (Das et al., 2011), whereas the pro-tumorigenic effects of JNK on HCC are associated with inflammation and require JNK function in non-parenchymal cells such as myeloid cells (Han et al., 2016) and hematopoietic cells (Cubero et al., 2015). Thus, the role of JNK in HCC might depend on the subtype and cellular context. Retrospective analysis of patient disease histories found no correlation of JNK activity in HCC with pathophysiological features (Hui et al., 2008). Moreover, continuous efforts with next-generation sequencing (NGS) have shown that the JNK pathway is not recurrently amplified in virus-, alcohol-, and other risk-factor-associated HCCs (Guichard et al., 2012; Huang et al., 2012; Jhunjhunwala et al., 2014; Schulze et al., 2015). Interestingly, recent NGS characterization of human pediatric liver cancers induced by intrahepatic cholestasis has shown massive gene amplification and rearrangements frequently targeting direct regulators of JNK (Iannelli et al., 2014). This suggests that the mechanistic involvement of JNK in the development of liver cancers is largely context dependent. Supporting this notion, HCCs from *Mdr2*-KO mice, a model of defects in hepatocyte biliary transporter, show similar genetic profiles affecting JNK activity as human pediatric liver cancers (Iannelli et al., 2014).

Our model of chronic cholestasis induced by oxidative stress further highlights that different disease etiologies have distinct impacts on signaling reliance and tumor phenotypes. In addition to the reported roles of JNK in cell proliferation, survival, apoptosis, and necrosis, as well as a lineage determinant role of JNK in liver parenchymal cells may also exist, where it not only favors proliferation of biliary cells but also directly biases biliary cell fate decisions in bipotential hepatic cells (Figure 8D). Importantly, we and others observed that

JNK inhibition retards ICC progression. Therefore, ICC patients and HCC patients with hepatobiliary abnormalities may preferentially benefit from JNK inhibition. Thus, stratifying liver cancers by disease etiologies may have great implications for preclinical studies with JNK inhibitors for targeted therapy.

One remaining question is the origin of the Cre-recombinase^{-}/Hspd1^{+} escaper cells. Using different lineage-tracing systems, several groups have failed to demonstrate a significant contribution of adult biliary-derived liver progenitor cells (LPCs) to hepatocyte neogenesis in diet or injury-induced mouse models (Jors et al., 2015; Tarlow et al., 2014; Yanger et al., 2014). However, LPC-mediated liver regeneration may require complete hepatocyte growth arrest of the hepatocyte and biliary compartment, as recently proposed (Lu et al., 2015). In our model, it remains unclear whether Hspd1^{+} ICC cells arise from LPCs, from dedifferentiated Sox9^{+} hepatocytes, and/or cholangiocytes. Indeed, recent studies propose that either of the latter two cell types can potentially contribute to ICC development (Fan et al., 2012; Guest et al., 2014; Saha et al., 2014; Tschaharganeh et al., 2014; Yimlamai et al., 2014; Zender et al., 2013). Further lineage-tracing studies should clarify this open question.

In conclusion, we show that Tnf is a key molecule driving cholangiocellular overgrowth and cancer development. In addition to the known signaling molecules implicated in ICC growth, such as Notch and Wnt, non-parenchymal cell-derived inflammatory signals can be added. As a reciprocal supportive interplay between cancer cells and their niche may be critical to promote cancer initiation and progression, our finding not only provides an example of a mechanism in which a pro-inflammatory microenvironment can function as pre-carcinogenic niche but also suggests the ROS/Tnf/JNK axis as an attractive ICC therapeutic target.

STAR★METHODS

CONTACT FOR REAGENT AND RESOURCE SHARING

Further information and requests for resources and reagents should be directed to and will be fulfilled by the Lead Contact, Mathias Heikenwalder (heikenwaelder@helmholtz-muenchen.de or m.heikenwaelder@dkfz-heidelberg.de).

EXPERIMENTAL MODEL AND SUBJECT DETAILS

Mice—Mice were maintained under SPF conditions. Experiments were conducted in accordance with the guidelines of the Germany Animal Protection Law and were approved by local committees of government of Bavaria (license number: 55.2–1-54–2532-134–14; license number: 55.2–1-54–2532-118–2016) and the government of Baden-Würrtemberg (license number: 35–9185.81/G178/16). C57BL/6J mice were purchased from Harlan or bred in-house. R26R-Confetti mice and Tnfr1KO mice were purchased from The Jackson Laboratory. Conditional *Hspd1* knockout mice were generated by Taconic-Artemis (Cologne, Germany) in close collaboration with the Chair of Nutrition and Immunology. Both male and female mice were used in all mouse experiments and no gender disparity was found when it came to the phenotype of Hspd1$^{\Delta LPC}$ mice or intercrossings of the latter. Diet-induced liver injury models and BDL model were provided by Prof. Geisler (Jors et al.,

2015). HDTV induced ICC models (license number: G178/16) were generated as previously described (Matter et al., 2016). AAV mediated Cre expression in hepatocytes were done by i.v. injection of 4×10^{11} viral genomes of AAV8-Ttr-Cre, purchased from VectorBiolabs, into 6–8-week-old male mice. We analyzed between 3 and 6 mice per condition in each experiment.

Human Material—Formalin-fixed, paraffin-embedded human liver tissue samples were retrieved from the archives and the biobank of the Institute of Surgical Pathology, University Hospital Zurich, Northwestern and Central Switzerland (EKNZ), and Faculty of Medicine, University Hospital RWTH Aachen, for morphological, immunohistological and molecular analyses. The study was approved by the local ethics committee ("Kantonale Ethikkommission Zürich", application number StV26/2005 and KEK-ZH-Nr. 2013–0382; EKNZ, application number 310/13; University Hospital RWTH Aachen, application number EK122/16).

Cell Lines and Primary Cultures

Isolation, Culture and Differentiation of Hepatoblasts: Isolation of fetal livers (C57BL/6J) at gestation stage E14.5 was done by a modified MACS based immune-isolation protocol (Nitou et al., 2002). Briefly, fetal livers were dissected, freed of adherent tissue, shredded and subsequently incubated with dispase II (1.6 U/ml) (Sigma) for 1hour at 37°C. Liver specimen were further dispersed by pipetting and filtered three times through a 100 μm Nylon cell strainer (Falcon). The cell suspension was further centrifuges for 10 min at 800 rpm, washed twice using Hepes-buffered (20 mM) (Sigma) DMEM (Dulbecco's Modified Eagle Medium; Gibco) with 0.01% DNase (Roche), and subsequently re-suspended in Hepes-buffered (20 mM) (Sigma) DMEM (Dulbecco's Modified Eagle Medium; Gibco) supplemented with 10% FBS (Biochrom) and 1x PenStrep (Life Technologies). Purification of E-Cadherin$^+$ hepatoblasts was performed using the rat anti-mouse E-Cadherin antibody (clone Decma-1, Merck Millipore). Briefly, anti-rat IgG microbeads were incubated with Decma-1 antibody for 45 min at room temperature on a Intelli-mixer (LTF Labortechnik) and the complexes of primary and secondary antibody were subsequently washed twice times with DMEM (Dulbecco's Modified Eagle Medium; Gibco) supplemented with 10% FBS (Biochrom) and 1x PenStrep (Life Technologies) using a table centrifuge for 10min at 13 rpm. Following the incubation of the cell suspension with the complexed microbeads, the cells were purified using the MACS columns (MS, Milteny Biotec). Cells were washed and afterwards eluded in Hepes-buffered (20 mM) (Sigma) DMEM (Dulbecco's Modified Eagle Medium; Gibco).

Isolated hepatocytes were plated onto rat tail type I collagen (Sigma) coated plates. Cells were kept in an undifferentiated state in basal medium composed of Williams' Medium E supplemented with 10% FCS, 10mM nicotinamide, 20 ng/ml mouse Egf (Roche Diagnostics), and 40 IU / ml insulin (Sigma Chemical Company). After 3 days, 0.5% DMSO or 10 ng/ml of recombinant murine Tnf was added into the basal medium to induce differentiation. For JNK inhibition in presence of Tnf, 10 μM of SP600125 (Abcam) was added. Cells were kept in basal medium or differentiation medium for another 7 days until harvest, changing the culture medium daily.

Isolation and Cultivation of Cholangiocytes: Ducts were isolated from 8–10 weeks old mice by microdissection (Keitel et al., 2010). The isolated bile ducts were cut into 3–4 mm segments, placed in a collagen matrix and covered with growth factor-containing medium. After 10–14 days cholangiocytes grew out of the ducts forming a monolayer. Cells were passaged once 80% confluent and cells were used in passages 4–9.

Isolation and Culture of Primary Hepatocytes: Male 8–12-week old C57Bl/6 mice were anesthetized by i.p. injection of 100 mg kg−1 body weight ketamine hydrochloride and 5 mg kg−1 body weight xylazine hydrochloride. After opening the abdominal cavity, the liver was perfused at 37 °C with HANKS buffer, supplemented with 1mM EDTA, via the portal vein for 5 min and subsequently with HANKS buffer, supplemented with 0,3 mg/ml Collagenase IV (Roche) and 10% glucose, for 5–7 min until disintegration of the liver structure was observed. The liver capsule was removed and the cell suspension was filtered through a 100 μm mesh. The cells were washed and, subsequently, viability of cells was determined by trypan blue staining. 1×10^5 living cells per well were seeded on collagen I-coated 12-well plates and cultured in Williams E medium (Life Technologies, Glutamax) supplemented with 2% fetal calf serum, 100 μg/ml penicillin/streptomycin.

Isolation and Culture of Primary Kupffer Cells: C57Bl/6 mice were heart perfused with HBSS. Liver lobes were collected and processed for flow cytometry. To obtain single-cell suspensions, organs were homogenized and incubated for 45 min in RPMI containing 60U Collagenase IV (Sigma) and 25 μg/ml DNase I (Sigma). Cell suspensions were washed with HBSS and layered upon 25%/50% percoll for gradient centrifugation (1800g/15min). Middle layers containing leukocytes were collected and washed twice in HBSS. Fc receptors were blocked by incubating cells in 5% FCS with purified mouse IgG (500 mg/ml, Jackson ImmunoResearch Laboratories). Stainings were performed in 5% FCS on ice for 30 min with optimal dilutions of commercially-prepared Lin (CD4 BV421 (GK1.5), CD8 BV421 (53–6.7), CD19 BV421 (6d5), Ter119 BV421 (Ter119)), F4/80 BV711 (BM8) (BioLegend), CD11b PE-Cy7 (M1/70), CD45 Alexa700 (30-F11) (eBioscience), Ly6G-PerCP5.5 (1A8) (BD Pharmingen). $Lin^-Ly6G^-Ly6C^-CD45^+CD11b^{int}F4/80^{hi}$ Kupffer cells were sorted on a BD FacsARIA III. After sortimg, 3×10^3 Kupffer cells were seeded on a 96-well plate and cultured in DMEM medium supplemented with 10% fetal calf serum, 1% non-essential amino acid and 100 μg/ml penicillin/streptomycin.

Isolation of Murine Liver Cells: Liver cells were isolated from 6–8 weeks old mice. For isolation, animals were sacrificed and liver was perfused via the inferior vena cava with EGTA containing buffer followed by a buffer containing collagenase (0,12 U/ml type NB 4G collagenase (Serva, Germany)). Liver was removed and mechanically disrupted. Cells suspension was centrifuged at 20g for 5 min. Pellet was washed and subjected to Percoll gradient (GE healthcare, Sweden). Hepatocytes were cultured on collagen-coated (Serva, Germany) plates in Williams'E medium supplemented with Pen/Strep, Gentamycin, 0,22 mM Glutamin, 0,02M HEPES, Insulin, 110nM Hydrocortison and 1,6% DMSO. The supernatant was subjected to Nycodenz gradient and the cells used for fluorescence-activated cell sorting.

Cell Lines and Drug Treatment: Human ICC cell lines, HuCCT-1 and ETK-1, and Mouse ICC cell line were generously provided by Dr. Roland Rad. Human HCC cell lines, HepG2 and Huh-7 were routinely maintained in our lab. The three ICC cell lines were cultured in RPMI medium supplemented with 10% fetal calf serum, 1% non-essential amino acid and 100 μg/ml penicillin/streptomycin. The two HCC cell lines were maintained in DMEM medium supplemented with 10% fetal calf serum, 1% non-essential amino acid and 100 μg/ml penicillin/streptomycin. For treatment with SP600125 (Abcam), JNK-IN-8 (Merck) or JNK6o (Bio-techne), 800 ~ 1,000 cells/well were seeded in 96-well plates. SP600125 (10, 20, 30 and 60 μM), JNK-IN-8 (1, 5, and 10 μM) or JNK6o (1, 5, and 10 μM) was added into the culture medium from the second day for 72 hours. Cell viability assay was performed using a CellTiter-Blue Cell Viability Assay (Promega) following the manufacturer's instruction. Primary Hepatocytes were treated with 2μM H_2O_2 for 6h. Subsequently, supernatant was collected and used for further treatment of primary Kupffer cells and Raw 246.7 cells. Primary Kupffer cells/well were treated with respective hepatocyte supernatants for 16h. Raw 246.7 cells were cultured in DMEM medium supplemented with 10% fetal calf serum, 1% non-essential amino acid and 100 μg/ml penicillin/streptomycin. 3×10^5 Raw 246.7 cells were seeded in 12-well plates and were either left untreated or were pretreated for 4h with the Inhibitors S3I-201 (working conc. 80μM, Biovision), LY-294002 (working conc. 50μM, Sigma), Isoliquiritigenin (working conc. 10μM, Sigma), TPCA-1 (working conc. 5μM, Sigma) or for 24h with MYD88 Inhibitor Peptide Set (NBP2–29328, working conc. 100μM, Novus Biologicals) respectively, before treatment with respective hepatocyte supernatants for 16h. Raw 246.7 cells were well tolerated under the treatment of the inhibitions without showing major cell death.

METHOD DETAILS

Subcutaneous Transplantation of Liver Tissue—The donor liver tissue of $Hspd1^{\Delta LPC}$ mice for the subcutaneous transplantation was prepared under sterile conditions. The recipient SCID Beige mice at the age of 4–8 weeks were anesthetized with Ketamin (100 mg/kg) and Rompun (10 mg/kg) under sterile conditions as well. For transplantation, a small incision into the previous disinfected skin of the back of the recipient mouse was used to place the minced donor tissue under the skin. For each of both flanks one tissue sample (3–4 mm in diameter) was transplanted. In total 12 transplantations on 6 mice were set up from 3 independent donors. Afterwards the incision was closed and disinfected again. Tumors were harvested 4–8 weeks after transplantation and fixed in 4% PFA in PBS, followed by immune-histochemical analysis.

Immunofluorescence Microscopy—Deparaffinized and rehydrated slides were subjected to microwave antigen retrieval in 25 mM citrate buffer (pH 6.0) and allowed to cool to room temperature. Antigen retrieval for F4/80 was performed by incubation with 1mg/ml Pronase XXIV (Sigma) for 10 minutes at room temperature. Slides were blocked in TBS containing 0.1% Triton X-100 and 2% serum from the species that the secondary antibody was raised in at room temperature for two hours. After blocking, primary antibodies diluted in TBS with 0.1% Triton X-100 and 2% blocking serum were added overnight at 4°C. After extensive washing, slides were incubated with the secondary antibody in TBS with 0.1% Triton X-100 and 2% blocking serum for 2 hours at room

temperature in dark and counterstaining with DAPI. Slides were mounted with Fluoromount-G (SouthernBiotech, Birmingham, Alabama, USA) and images were captured with Olympus FV10i confocal Microscope (Olympus, Germany).

Electron Microscopy—Liver tissues were fixed with 4% glutaraldehyde in PBS for less than 24 h and embedded in Epon. The tissues were then trimmed and reoriented so that ultrathin sections could be cut and treated with 1% uranyl acetate and lead citrate. Electron micrographs were obtained using a Philips CM 100 electron microscope.

RNA In-Situ Hybridization—Probes for Tnf, Tnfr1, the housekeeping gene ubiquitin C (positive control), the bacterial gene dapB (negative control), and the hybridization kit (RNAscope 2.0 FFPE Assay) were purchased from Advanced Cell Diagnostics. RNA in-situ hybridization was performed using the RNAscope 2.0 technology according to the manufacturer instructions. Briefly, 2 μm paraffin sections were pretreated with heat at 75°C in EZprep buffer for 20 minutes and protease at 37°C for 30 minutes. Tnfr1 specific probe pairs (Advanced Cell Diagnostics) were then hybridized at 48°C for 2 hours, followed by a series of signal amplification and washing steps. Hybridization signals were detected by DAB staining, followed by counterstaining with hematoxylin. For fluorescent in situ, 4 μm sections were pretreated by boiling with pretreat 2 for 30 minutes followed by incubation with pretreat 4 at 40°C for 35 minutes. Tnf specific probe pairs were then hybridized at 40°C for 2 hours. Stained slides were scanned into digital images using a Leica SCN400 scanner (Leica) at ×40 magnification.

BrdU Assay—For proliferation experiments cholangiocytes were seeded on collagen-coated 96 well plates (confluence of the cells: 30–40%). After 24 hours cells were washed 2 times with starvation medium and stimulated with various substances for another 36 hr. 24 hr prior to end of the experiment the cells were additionally treated with BrdU. The BrdU-assay was carried out according to the manufacturer's protocol (BrdU Roche). SP600125, JNK-IN-8 or JNK6o was added 30 min prior to the stimulation with Tnf.

Histology and Immunohistochemistry—Liver tissue samples were fixed overnight in 4% paraformaldehyde, embedded in paraffin. Paraffin sections were subjected to hematoxylin-eosin or immunohistochemistry staining as previously described (Haybaeck et al., 2009). Briefly, paraffin sections (2 μm) and frozen sections (5 μm) of livers were used for automated staining performed on Bond MAX (Leica) using the DAB detection kit (bornmax). The following primary antibodies were used: mouse anti-8-OHdG (1:1000 dilution, Abcam); goat anti-Afp (1:1000 dilution, R&D); rabbit anti-CHOP (1:1000 dilution, Cell Signaling); rabbit anti-c-Jun (1:1000 dilution, Cell Signaling); p-c-Jun (1:1000 dilution, Cell Signaling); rabbit anti-cleaved Caspase-3 (1:1000 dilution, Cell Signaling); rabbit anti-Collagen type IV (1:1000 dilution, Cedarlane); rabbit anti-Cytokeratin (1:1000 dilution, Dako); rat anti-F4/80 (1:1000 dilution, BioLegend); rabbit anti-Glutamine Synthetase (1:1000 dilution, Abcam); goat anti-Hspd1 (1:4000 dilution, Santa Cruz); rabbit anti-Ki67 (1:200 dilution, NeoMarkers); rat anti-Ly6G (1:1000 dilution, BD); rabbit anti-RelA (1:200 dilution NeoMarkers); rabbit anti-Tnf (1:150 dilution, Abcam); rabbit anti-c-Myc (1:1000 dilution, Abcam); rat anti-CK19 (1:100 dilution, Developmental Studies Hybridoma Bank).

Paraffin-embedded tissue sections were used for staining with 0.1% Sirius red dissolved in saturated picric acid. Oval cell proliferation was detected by A6 staining (1:50), kindly provided by Dr. Valentina Factor. TUNEL assays were performed using the Fluorescein cell death detection kit (Clontech).

Measurement of Serum Parameters—The analysis for AST, ALT, AP, bilirubin, cholesterol, triglycerides and bile acid was performed with mouse serum on a Roche Modular System (Roche Diagnostics) with a commercially available automated colorimetric system using a Hitachi P-Modul (Roche).

ELISA

Tnf protein levels from liver homogenates were measured using a Quantikine-Elisa-Kit from R&D Systems (Oxon, UK). IL6 protein levels were measured using a mouse IL6 Elisa kit from RayBiotech (GA, US). The procedures closely followed the manufacturer's instructions. The detection limit was 16 pg/ml for Tnf and 2 pg/ml for IL6 respectively. The homogenization buffer was tested as a negative control.

Immunoblot Analysis—Liver homogenates were prepared by mechanical grinding in RIPA buffer (50 mM Tris; 1% NP40; 0.25% Deoxycholic acid sodium salt; 150 mM NaCl; 1 mM EGTA) containing Halt Protease and Phosphatase Inhibitor Cocktail (Thermo Scientific), and quantified with a BCA protein assay kit (Thermo Scientific) according to the manufacturer's manual. 50 μg protein were denatured in Laemmli buffer containing 5% β-mercaptoethanol and separated by gel electrophoresis and blotted by wet blotting onto nitrocellulose membranes (Bio Rad). Membranes were blocked in 5% milk/TBS-T for at least 1hr at RT. Primary antibodies against Hspd1 (Santa Cruz), Pcna (Santa Cruz), Gp73 (Santa Cruz), c-Jun (Abcam), p-c-Jun (Cell Signaling), p-JNK, JNK, p-Erk1/2, Erk1/2, CHOP, p-p38 MAPK, p38 MAPK, p-Akt, Akt and Gapdh (all Cell Signaling) and were incubated at 4°C overnight under shaking conditions. Incubation with the secondary antibody (HRP-anti rabbit IgG, 1:10000, HRP-anti mouse IgG, 1:10000, Jackson; HRP-anti Goat IgG, 1:10000, Dako) was performed under shaking conditions for 1 hr. Detection was achieved with Clarity Western ECL Substrate (Bio Rad) using Stella 3200 imaging system (Bio Rad). To assure equal loading, membranes reprobed with anti-Gapdh antibody (Cell Signaling) and detected as described above.

RNA Isolation from Liver Tissue—Total RNA from mouse liver samples or cultured cells was isolated using RNeasy Mini kit (Qiagen). The quantity and quality of the RNA was determined spectroscopically using a nanodrop (Thermo Scientific). Purified RNA was reversely transcribed into cDNA using Quantitect Reverse Transcription Kit (Qiagen) according to the manufacturer's instructions.

Array-based Comparative Genomic Hybridization (aCGH)—200 ng of isolated DNA were amplified using the REPLI-g Whole Genome Amplification Kit (Qiagen, Hilden, Germany) according to the manufacturer's instructions. Efficiency of amplification of high molecular weight DNA was controlled by agarose gel electrophoresis. 3 ug of amplified DNA were digested by Rsa I and Alu I for 2h at 37°C. Digested DNA was subsequently

purified using QIAprep Spin Miniprep Columns (Qiagen, Hilden, Germany). Briefly, the digestion reaction was mixed with 5 volumes buffer PB and loaded onto the column. The column was washed once with buffer PE and DNA fragments eluted in buffer EB. 1 μg amplified sample DNA and sex-matched reference DNA was labeled with Cy3 or Cy5, respectively, using the SureTag DNA Labeling Kit (Agilent, Santa Clara, CA) according to the manufacturer's instructions (protocol version 7.3). Labeled DNA was subsequently hybridized on Mouse Genome CGH 1 × 244K Oligo Microarrays (Agilent, Santa Clara, CA) for 40h. After washing slides were processed on an Agilent G2565BA scanner. Agilent Technologies' Feature Extraction (version 10.7.3.1) was used for data quality control and extraction. aCGH analysis and plotting was performed as described in (Vucur et al., 2013). In order to reduce GC wave patterns of the resulting profiles the NoWaves approach was used. For this purpose a reference data set consisting of 10 normal-tissue profiles was generated. The synteny analysis between mouse and human was conducted as described in Wolf et al. (2014). Matching of mouse copy number changes to syntenic human regions that were also changed in copy number was tested for random occurrence using Fisher's exact test. Copy number profiles of human intrahepatic cholangiocarcinomas were generated from level 3 segmented data downloaded from The Cancer Genome Atlas (TCGA http://cancergenome.nih.gov/) CHOL dataset. R packages used for aCGH and synteny analysis were as follows: CGHcall, CGHregions and RCircos.

Real-time PCR—For mRNA expression analysis quantitative real-time PCR was performed in triplicates in 384-well plates using Fast Start SYBR Green Master Rox (Roche) on a 7900 HT qPCR system (Applied Biosystems, Life Technologies Darmstadt, Germany). Relative mRNA levels were calculated according to the ΔΔCt relative quantification method and were normalized to at least two of the examined house-keeping genes (Hprt; Rhot2; Gapdh) levels.

QUANTIFICATION AND STATISTICAL ANALYSIS

Counting of Proliferating Hepatocytes—For quantification of Ki67 staining, slides were scanned using a SCN400 slide scanner (Leica). The total number of $Ki67^+$ hepatocytes was counted at the screen (20 x). For each mouse 5 fields were counted.

Statistical Analysis—Statistical analyses were performed with Prism software (Graphpad Prism version 5.0a). The standard error of the mean was calculated from the average of at least 3 independent samples per condition. To evaluate statistical significance, data was subjected to Student's t-test (unpaired, two-tailed test). Human specimens were compared using the chi-square test. A p value of less than 0.05 was considered significant.

DATA AND SOFTWARE AVAILABILITY

The accession number for the aCGH data reported in this paper is array express: E-MTAB-4624.

Supplementary Material

Refer to Web version on PubMed Central for supplementary material.

ACKNOWLEDGMENTS

We thank Ruth Hillermann, Olga Seelbach, Robert Baier, Reiner Dunkl, Tjeerd Sijmonsma, Danijela Heide, Jenny Hetzer, Daniel Kull, and Fiona Mayer for technical support. We thank Jan Tchorz for constructive suggestions. This work was supported by the Horizon 2020 HEPCAR, the ERC Consolidator grant "HepatoMetaboPath", the SFB Transregio SFB/TR36, the SFB/TR179, the SFB/TR209, and the Graduiertenkolleg (GRK482) to M.H. and D.H., DFG grant (GE 2289/1) to F.G., and NIH grant DK107220 to R.J.D. A.W. was supported by grants from the Hartmann Müller Stiftung and the Swiss National Science Foundation (SNF) (grant SNF 310030_146940).

REFERENCES

Ariizumi SI, and Yamamoto M (2014). Intrahepatic cholangiocarcinoma and cholangiolocellular carcinoma in cirrhosis and chronic viral hepatitis. Surg. Today 45, 682–687. [PubMed: 25253466]

Arnott CH, Scott KA, Moore RJ, Robinson SC, Thompson RG, and Balkwill FR (2004). Expression of both TNF-alpha receptor subtypes is essential for optimal skin tumour development. Oncogene 23, 1902–1910. [PubMed: 14661063]

Berger E, Yuan D, Waldschmitt N, Rath E, Allgäuer M, Staszewski O, Kober O, Lobner E, Schöttl T, Prinz M, et al. (2016). Mitochondrial function controls epithelial stemness and proliferation in the intestine independent of unfolded protein response signaling mechanisms. Nat. Commun 7, 13171. [PubMed: 27786175]

Boulter L, Govaere O, Bird TG, Radulescu S, Ramachandran P, Pellicoro A, Ridgway RA, Seo SS, Spee B, Van Rooijen N, et al. (2012). Macrophage-derived Wnt opposes Notch signaling to specify hepatic progenitor cell fate in chronic liver disease. Nat. Med 18, 572–579. [PubMed: 22388089]

Boulter L, Guest RV, Kendall TJ, Wilson DH, Wojtacha D, Robson AJ, Ridgway RA, Samuel K, Van Rooijen N, Barry ST, et al. (2015). WNT signaling drives cholangiocarcinoma growth and can be pharmacologically inhibited. J. Clin. Invest 125, 1269–1285. [PubMed: 25689248]

Cubero FJ, Zhao G, Nevzorova YA, Hatting M, Al Masaoudi M, Verdier J, Peng J, Schaefer FM, Hermanns N, Boekschoten MV, et al. (2015). Haematopoietic cell-derived Jnk1 is crucial for chronic inflammation and carcinogenesis in an experimental model of liver injury. J. Hepatol 62, 140–149. [PubMed: 25173965]

Das M, Garlick DS, Greiner DL, and Davis RJ (2011). The role of JNK in the development of hepatocellular carcinoma. Genes Dev. 25, 634–645. [PubMed: 21406557]

Espin-Palazon R, Stachura DL, Campbell CA, Garcia-Moreno D, Del Cid N, Kim AD, Candel S, Meseguer J, Mulero V, and Traver D (2014). Proinflammatory signaling regulates hematopoietic stem cell emergence. Cell 159, 1070–1085. [PubMed: 25416946]

Fan B, Malato Y, Calvisi DF, Naqvi S, Razumilava N, Ribback S, Gores GJ, Dombrowski F, Evert M, Chen X, et al. (2012). Cholangiocarcinomas can originate from hepatocytes in mice. J. Clin. Invest 122, 2911–2915. [PubMed: 22797301]

Fujimoto A, Furuta M, Shiraishi Y, Gotoh K, Kawakami Y, Arihiro K, Nakamura T, Ueno M, Ariizumi S, Hai Nguyen H, et al. (2015). Whole-genome mutational landscape of liver cancers displaying biliary phenotype reveals hepatitis impact and molecular diversity. Nat. Commun 6, 6120. [PubMed: 25636086]

Gatto M, and Alvaro D (2010). New insights on cholangiocarcinoma. World J. Gastrointest. Oncol 2, 136–145. [PubMed: 21160821]

Guest RV, Boulter L, Kendall TJ, Minnis-Lyons SE, Walker R, Wigmore SJ, Sansom OJ, and Forbes SJ (2014). Cell lineage tracing reveals a biliary origin of intrahepatic cholangiocarcinoma. Cancer Res. 74, 1005–1010. [PubMed: 24310400]

Guichard C, Amaddeo G, Imbeaud S, Ladeiro Y, Pelletier L, Maad IB, Calderaro J, Bioulac-Sage P, Letexier M, Degos F, et al. (2012). Integrated analysis of somatic mutations and focal copy-number changes identifies key genes and pathways in hepatocellular carcinoma. Nat. Genet 44, 694–698. [PubMed: 22561517]

Han MS, Barrett T, Brehm MA, and Davis RJ (2016). Inflammation mediated by JNK in myeloid cells promotes the development of hepatitis and hepatocellular carcinoma. Cell Rep. 15, 19–26. [PubMed: 27052181]

Haybaeck J, Zeller N, Wolf MJ, Weber A, Wagner U, Kurrer MO, Bremer J, Iezzi G, Graf R, Clavien PA, et al. (2009). A lymphotoxin-driven pathway to hepatocellular carcinoma. Cancer Cell 16, 295–308. [PubMed: 19800575]

Hefetz-Sela S, Stein I, Klieger Y, Porat R, Sade-Feldman M, Zreik F, Nagler A, Pappo O, Quagliata L, Dazert E, et al. (2014). Acquisition of an immunosuppressive protumorigenic macrophage phenotype depending on c-Jun phosphorylation. Proc. Natl. Acad. Sci. USA 111, 17582–17587. [PubMed: 25422452]

Huang J, Deng Q, Wang Q, Li KY, Dai JH, Li N, Zhu ZD, Zhou B, Liu XY, Liu RF, et al. (2012). Exome sequencing of hepatitis B virus-associated hepatocellular carcinoma. Nat. Genet 44, 1117–1121. [PubMed: 22922871]

Huang H, Chen HW, Evankovich J, Yan W, Rosborough BR, Nace GW, Ding Q, Loughran P, Beer-Stolz D, Billiar TR, et al. (2013). Histones activate the NLRP3 inflammasome in Kupffer cells during sterile inflammatory liver injury. J. Immunol 191, 2665–2679. [PubMed: 23904166]

Hui L, Bakiri L, Mairhorfer A, Schweifer N, Haslinger C, Kenner L, Komnenovic V, Scheuch H, Beug H, and Wagner EF (2007). p38alpha suppresses normal and cancer cell proliferation by antagonizing the JNK-c-Jun pathway. Nat. Genet 39, 741–749. [PubMed: 17468757]

Hui L, Zatloukal K, Scheuch H, Stepniak E, and Wagner EF (2008). Proliferation of human HCC cells and chemically induced mouse liver cancers requires JNK1-dependent p21 downregulation. J. Clin. Invest 118, 3943–3953. [PubMed: 19033664]

Iannelli F, Collino A, Sinha S, Radaelli E, Nicoli P, D'Antiga L, Sonzogni A, Faivre J, Buendia MA, Sturm E, et al. (2014). Massive gene amplification drives paediatric hepatocellular carcinoma caused by bile salt export pump deficiency. Nat. Commun 5, 3850. [PubMed: 24819516]

Jhunjhunwala S, Jiang Z, Stawiski EW, Gnad F, Liu J, Mayba O, Du P, Diao J, Johnson S, Wong KF, et al. (2014). Diverse modes of genomic alteration in hepatocellular carcinoma. Genome Biol. 15, 436. [PubMed: 25159915]

Jiao Y, Pawlik TM, Anders RA, Selaru FM, Streppel MM, Lucas DJ, Niknafs N, Guthrie VB, Maitra A, Argani P, et al. (2013). Exome sequencing identifies frequent inactivating mutations in BAP1, ARID1A and PBRM1 in intrahepatic cholangiocarcinomas. Nat. Genet 45, 1470–1473. [PubMed: 24185509]

Jors S, Jeliazkova P, Ringelhan M, Thalhammer J, Durl S, Ferrer J, Sander M, Heikenwalder M, Schmid RM, Siveke JT, et al. (2015). Lineage fate of ductular reactions in liver injury and carcinogenesis. J. Clin. Invest 125, 2445–2457. [PubMed: 25915586]

Kamata H, Honda S, Maeda S, Chang L, Hirata H, and Karin M (2005). Reactive oxygen species promote TNFalpha-induced death and sustained JNK activation by inhibiting MAP kinase phosphatases. Cell 120, 649–661. [PubMed: 15766528]

Kang LI, Mars WM, and Michalopoulos GK (2012). Signals and cells involved in regulating liver regeneration. Cells 1, 1261–1292. [PubMed: 24710554]

Keitel V, Ullmer C, and Haussinger D (2010). The membrane-bound bile acid receptor TGR5 (Gpbar-1) is localized in the primary cilium of cholangiocytes. Biol. Chem 391, 785–789. [PubMed: 20623999]

Liu B, Zupan B, Laird E, Klein S, Gleason G, Bozinoski M, Gal Toth J, and Toth M (2014). Maternal hematopoietic TNF, via milk chemokines, programs hippocampal development and memory. Nat. Neurosci 17, 97–105. [PubMed: 24292233]

Livet J, Weissman TA, Kang H, Draft RW, Lu J, Bennis RA, Sanes JR, and Lichtman JW (2007). Transgenic strategies for combinatorial expression of fluorescent proteins in the nervous system. Nature 450, 56–62. [PubMed: 17972876]

Lu WY, Bird TG, Boulter L, Tsuchiya A, Cole AM, Hay T, Guest RV, Wojtacha D, Man TY, Mackinnon A, et al. (2015). Hepatic progenitor cells of biliary origin with liver repopulation capacity. Nat. Cell Biol 17, 971–983. [PubMed: 26192438]

Maeda S, Kamata H, Luo JL, Leffert H, and Karin M (2005). IKKbeta couples hepatocyte death to cytokine-driven compensatory proliferation that promotes chemical hepatocarcinogenesis. Cell 121, 977–990. [PubMed: 15989949]

Malato Y, Naqvi S, Schurmann N, Ng R, Wang B, Zape J, Kay MA, Grimm D, and Willenbring H (2011). Fate tracing of mature hepatocytes in mouse liver homeostasis and regeneration. J. Clin. Invest 121, 4850–4860. [PubMed: 22105172]

Matter MS, Marquardt JU, Andersen JB, Quintavalle C, Korokhov N, Stauffer JK, Kaji K, Decaens T, Quagliata L, Elloumi F, et al. (2016). Oncogenic driver genes and the inflammatory microenvironment dictate liver tumor phenotype. Hepatology 63, 1888–1899. [PubMed: 26844528]

Nakagawa H, Umemura A, Taniguchi K, Font-Burgada J, Dhar D, Ogata H, Zhong Z, Valasek MA, Seki E, Hidalgo J, et al. (2014). ER stress co-operates with hypernutrition to trigger TNF-dependent spontaneous HCC development. Cancer Cell 26, 331–343. [PubMed: 25132496]

Nishikawa Y, Sone M, Nagahama Y, Kumagai E, Doi Y, Omori Y, Yoshioka T, Tokairin T, Yoshida M, Yamamoto Y, et al. (2013). Tumor necrosis factor-alpha promotes bile ductular transdifferentiation of mature rat hepatocytes in vitro. J. Cell Biochem 114, 831–843. [PubMed: 23097189]

Nitou M, Sugiyama Y, Ishikawa K, and Shiojiri N (2002). Purification of fetal mouse hepatoblasts by magnetic beads coated with monoclonal anti-e-cadherin antibodies and their in vitro culture. Exp. Cell Res 279, 330–343. [PubMed: 12243758]

Ohsawa S, Sato Y, Enomoto M, Nakamura M, Betsumiya A, and Igaki T (2012). Mitochondrial defect drives non-autonomous tumour progression through Hippo signalling in *Drosophila*. Nature 490, 547–551. [PubMed: 23023132]

Pikarsky E, Porat RM, Stein I, Abramovitch R, Amit S, Kasem S, Gutkovich-Pyest E, Urieli-Shoval S, Galun E, and Ben-Neriah Y (2004). NF-kappaB functions as a tumour promoter in inflammation-associated cancer. Nature 431, 461–466. [PubMed: 15329734]

Postic C, Shiota M, Niswender KD, Jetton TL, Chen Y, Moates JM, Shelton KD, Lindner J, Cherrington AD, and Magnuson MA (1999). Dual roles for glucokinase in glucose homeostasis as determined by liver and pancreatic beta cell-specific gene knock-outs using Cre recombinase. J. Biol. Chem 274, 305–315. [PubMed: 9867845]

Rizvi S, Eaton JE, and Gores GJ (2015). Primary sclerosing cholangitis as a premalignant biliary tract disease: surveillance and management. Clin. Gastroenterol. Hepatol 13, 2152–2165. [PubMed: 26051390]

Roberts RA, Ganey PE, Ju C, Kamendulis LM, Rusyn I, and Klaunig JE (2007). Role of the Kupffer cell in mediating hepatic toxicity and carcinogenesis. Toxicol. Sci 96, 2–15. [PubMed: 17122412]

Rougemont AL, Genevay M, McKee TA, Gremaud M, Mentha G, and Rubbia-Brandt L (2010). Extensive biliary intraepithelial neoplasia (BilIN) and multifocal early intrahepatic cholangiocarcinoma in non-biliary cirrhosis. Virchows Arch. 456, 711–717. [PubMed: 20428886]

Saha SK, Parachoniak CA, Ghanta KS, Fitamant J, Ross KN, Najem MS, Gurumurthy S, Akbay EA, Sia D, Cornella H, et al. (2014). Mutant IDH inhibits HNF-4alpha to block hepatocyte differentiation and promote biliary cancer. Nature 513, 110–114. [PubMed: 25043045]

Sakurai T, Maeda S, Chang L, and Karin M (2006). Loss of hepatic NF-kappa B activity enhances chemical hepatocarcinogenesis through sustained c-Jun N-terminal kinase 1 activation. Proc. Natl. Acad. Sci. USA 103, 10544–10551. [PubMed: 16807293]

Scheeren FA, Kuo AH, van Weele LJ, Cai S, Glykofridis I, Sikandar SS, Zabala M, Qian D, Lam JS, Johnston D, et al. (2014). A cell-intrinsic role for TLR2-MYD88 in intestinal and breast epithelia and oncogenesis. Nat. Cell Biol 16, 1238–1248. [PubMed: 25362351]

Schulze K, Imbeaud S, Letouze E, Alexandrov LB, Calderaro J, Rebouissou S, Couchy G, Meiller C, Shinde J, Soysouvanh F, et al. (2015). Exome sequencing of hepatocellular carcinomas identifies new mutational signatures and potential therapeutic targets. Nat. Genet 47, 505–511. [PubMed: 25822088]

Shi Y, Evans JE, and Rock KL (2003). Molecular identification of a danger signal that alerts the immune system to dying cells. Nature 425, 516–521. [PubMed: 14520412]

Szabo G, and Petrasek J (2015). Inflammasome activation and function in liver disease. Nat. Rev. Gastroenterol. Hepatol 12, 387–400. [PubMed: 26055245]

Taniguchi K, Wu LW, Grivennikov SI, de Jong PR, Lian I, Yu FX, Wang K, Ho SB, Boland BS, Chang JT, et al. (2015). A gp130-Src-YAP module links inflammation to epithelial regeneration. Nature 519, 57–62. [PubMed: 25731159]

Tarlow BD, Pelz C, Naugler WE, Wakefield L, Wilson EM, Finegold MJ, and Grompe M (2014). Bipotential adult liver progenitors are derived from chronically injured mature hepatocytes. Cell Stem Cell 15, 605–618. [PubMed: 25312494]

Tschaharganeh DF, Xue W, Calvisi DF, Evert M, Michurina TV, Dow LE, Banito A, Katz SF, Kastenhuber ER, Weissmueller S, et al. (2014). p53-dependent Nestin regulation links tumor suppression to cellular plasticity in liver cancer. Cell 158, 579–592. [PubMed: 25083869]

Tyson GL, and El-Serag HB (2011). Risk factors for cholangiocarcinoma. Hepatology 54, 173–184. [PubMed: 21488076]

Vucur M, Reisinger F, Gautheron J, Janssen J, Roderburg C, Cardenas DV, Kreggenwinkel K, Koppe C, Hammerich L, Hakem R, et al. (2013). RIP3 inhibits inflammatory hepatocarcinogenesis but promotes cholestasis by controlling caspase-8- and JNK-dependent compensatory cell proliferation. Cell Rep 4, 776–790. [PubMed: 23972991]

Weber J, Ollinger R, Friedrich M, Ehmer U, Barenboim M, Steiger K, Heid I, Mueller S, Maresch R, Engleitner T, et al. (2015). CRISPR/Cas9 somatic multiplex-mutagenesis for high-throughput functional cancer genomics in mice. Proc. Natl. Acad. Sci. USA 112, 13982–13987. [PubMed: 26508638]

Wolf MJ, Adili A, Piotrowitz K, Abdullah Z, Boege Y, Stemmer K, Ringelhan M, Simonavicius N, Egger M, Wohlleber D, et al. (2014). Metabolic activation of intrahepatic CD8+ T cells and NKT cells causes nonalcoholic steatohepatitis and liver cancer via cross-talk with hepatocytes. Cancer Cell 26, 549–564. [PubMed: 25314080]

Woodworth CD, McMullin E, Iglesias M, and Plowman GD (1995). Interleukin 1 alpha and tumor necrosis factor alpha stimulate autocrine amphiregulin expression and proliferation of human papillomavirus-immortalized and carcinoma-derived cervical epithelial cells. Proc. Natl. Acad. Sci. USA 92, 2840–2844. [PubMed: 7708734]

Yanger K, Knigin D, Zong Y, Maggs L, Gu G, Akiyama H, Pikarsky E, and Stanger BZ (2014). Adult hepatocytes are generated by self-duplication rather than stem cell differentiation. Cell Stem Cell 15, 340–349. [PubMed: 25130492]

Yimlamai D, Christodoulou C, Galli GG, Yanger K, Pepe-Mooney B, Gurung B, Shrestha K, Cahan P, Stanger BZ, and Camargo FD (2014). Hippo pathway activity influences liver cell fate. Cell 157, 1324–1338. [PubMed: 24906150]

Zender S, Nickeleit I, Wuestefeld T, Sorensen I, Dauch D, Bozko P, El-Khatib M, Geffers R, Bektas H, Manns MP, et al. (2013). A critical role for notch signaling in the formation of cholangiocellular carcinomas. Cancer Cell 23, 784–795. [PubMed: 23727022]

Zhang F, Chen XP, Zhang W, Dong HH, Xiang S, Zhang WG, and Zhang BX (2008). Combined hepatocellular cholangiocarcinoma originating from hepatic progenitor cells: immunohistochemical and double-fluorescence immunostaining evidence. Histopathology 52, 224–232. [PubMed: 18184271]

Zhu HZ, Ruan YB, Wu ZB, and Zhang CM (2000). Kupffer cell and apoptosis in experimental HCC. World J. Gastroenterol 6, 405–407. [PubMed: 11819610]

Zou S, Li J, Zhou H, Frech C, Jiang X, Chu JS, Zhao X, Li Y, Li Q, Wang H, et al. (2014). Mutational landscape of intrahepatic cholangiocarcinoma. Nat. Commun 5, 5696. [PubMed: 25526346]

Highlights

- Hepatic mitochondrial dysfunction induces premalignant cholangiocellular lesions
- Hepatocytes under oxidative stress activate Tnf-producing Kupffer cells
- Kupffer cell-derived Tnf triggers cholangiocyte overgrowth through JNK
- JNK inhibition impairs intrahepatic cholangiocarcinoma development in several models

Significance

HCC and ICC are malignant, heterogeneous cancers with rising incidence, poor prognosis, and limited treatment options. The liver microenvironment might favor the development of either HCC or ICC. However, mechanistic underpinnings remain elusive. Analyses of distinct murine and human ICC and HCC specimens revealed especially high ROS levels within ICC and surrounding hepatocytes. Using a mouse model mimicking severe liver damage caused by mitochondrial dysfunction and high ROS levels, we induced profound compensatory proliferation of cholangiocytes and high, focal Tnf levels favoring cholangiocellular overgrowth and premalignant transformation. Our results indicate that Tnf fuels ICC through activation of Tnfr1/JNK in cholangiocytes. Deletion of JNK dampened ICC formation in several aggressive ICC models. Thus, targeting the ROS/Tnf/JNK axis might be promising for ICC therapy.

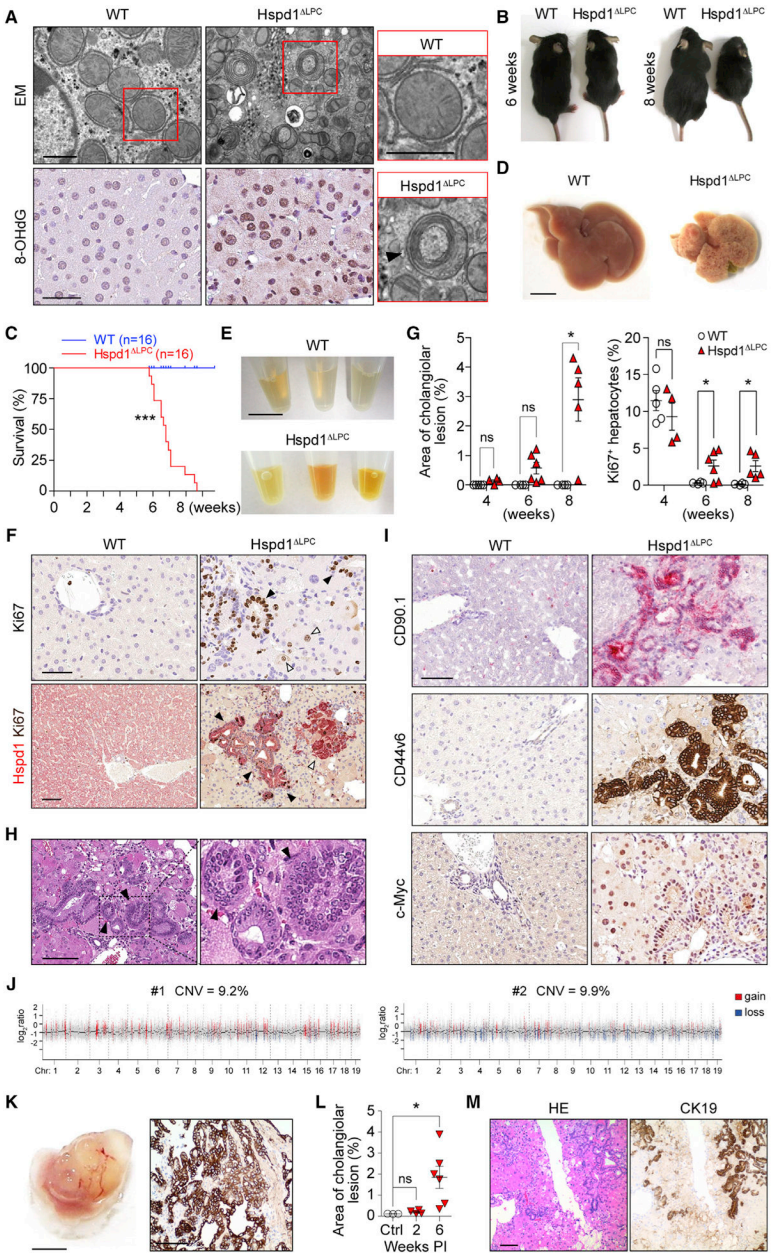

Figure 1. Lack of Hspd1 Causes Acute Liver Damage, Hepatic Proliferation, and Cholangiocellular Tumorigenesis

(A) Electron microscopy and 8-OHdG staining of WT and Hspd1$^{\Delta LPC}$ livers. Arrowhead indicates a classic mitophagosome. Scale bars, 0.5 μm (upper), 50 μm (lower).

(B) Six- and 8-week-old Hspd1$^{\Delta LPC}$ mice and WT littermates.

(C) Survival curve of Hspd1$^{\Delta LPC}$ and WT mice.

(D) Eight-week-old Hspd1$^{\Delta LPC}$ and WT littermate livers. Scale bar, 5 mm.

(E) Serum from 8-week-old Hspd1$^{\Delta LPC}$ mice and WT littermates. Scale bar, 1 cm.

(F) Upper: Ki67 staining of 6-week-old Hspd1$^{\Delta LPC}$ and WT livers. Black arrowheads, Ki67^{+} cholangiocytes; white arrowheads, Ki67^{+} hepatocytes. Lower: double staining of Hspd1 (red) and Ki67 (brown) of 8-week-old Hspd1$^{\Delta LPC}$ and WT livers, indicating foci of

hepatocyte (white arrowhead) and cholangiocellular (black arrowhead) proliferation. Scale bar, 50 μm.

(G) Quantification of cholangiocellular lesions and $Ki67^{+}$ hepatocytes over time in $Hspd1^{\Delta LPC}$ mice and WT littermates.

(H) H&E staining of $Hspd1^{\Delta LPC}$ liver. Arrowheads indicate biliary intraepithelial neoplasia. Scale bar, 100 μm.

(I) IHC analysis in 8-week-old WT and $Hspd1^{\Delta LPC}$ livers. Scale bar, 50 μm.

(J) Genomic hybridization profiles of $CK19^{+}$ cholangiocellular neoplasia.

(K) Macroscopy (left) and CK19 staining (right) of tumor graft from severe combined immunodeficiency Beige liver. Scale bars, 5 mm (left), 100 μm (right).

(L) Quantification of cholangiocellular lesions over time in AAV8-Cre $Hspd1^{loxP/loxP}$ and control mice.

(M) H&E and CK19 staining of AAV8-Cre $Hspd1^{loxP/loxP}$ livers. Scale bar, 100 μm.

Data are represented as the mean ± SEM. *$p < 0.05$, ***$p < 0.001$. ns, not significant. See also Figures S1 and S2.

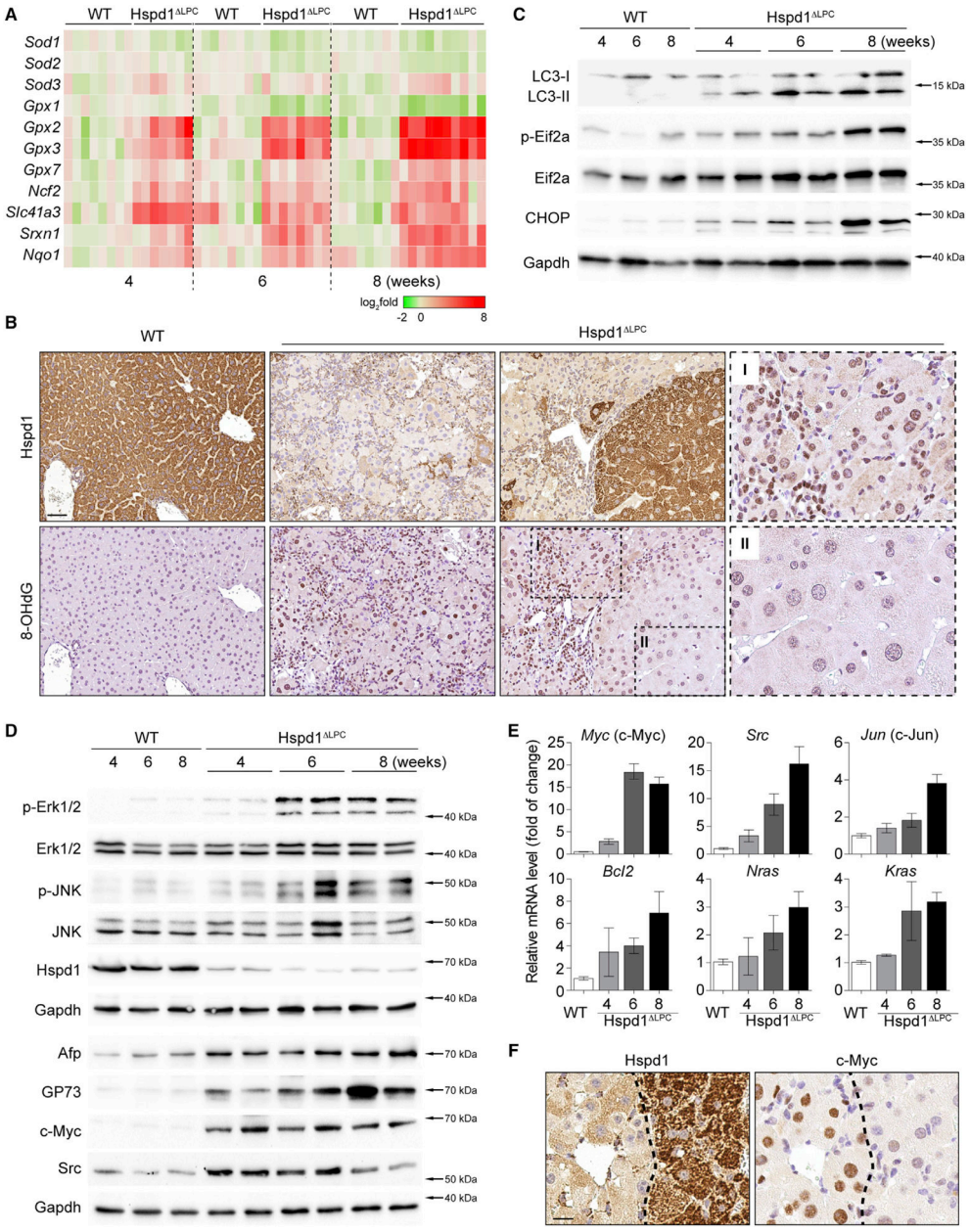

Figure 2. Oxidative and Pro-carcinogenic Liver Microenvironment in Hspd1$^{\Delta LPC}$ Mice

(A) Heatmap of the expression of anti-oxidant genes in Hspd1$^{\Delta LPC}$ livers compared with WT over time. Red, upregulated; green, downregulated.

(B) Hspd1 and 8-OHdG staining of 8-week-old Hspd1$^{\Delta LPC}$ and WT livers. Scale bar, 50 μm.

(C) Western blot analysis of Hspd1$^{\Delta LPC}$ and WT livers from the indicated ages.

(D) Western blot analysis of Hspd1$^{\Delta LPC}$ and WT livers from the indicated ages.

(E) qRT-PCR for the top upregulated pro-survival genes in Hspd1$^{\Delta LPC}$ liver compared with 8-week-old WT liver. Data are represented as the mean ± SEM.

(F) Hspd1 and c-Myc IHC in consecutive liver sections from 8-week-old WT and Hspd1$^{\Delta LPC}$ mice. The dashed lines indicate the border between the Hspd1^{+} and Hspd1^{-} areas. Scale bar, 20 μm.

See also Figure S3.

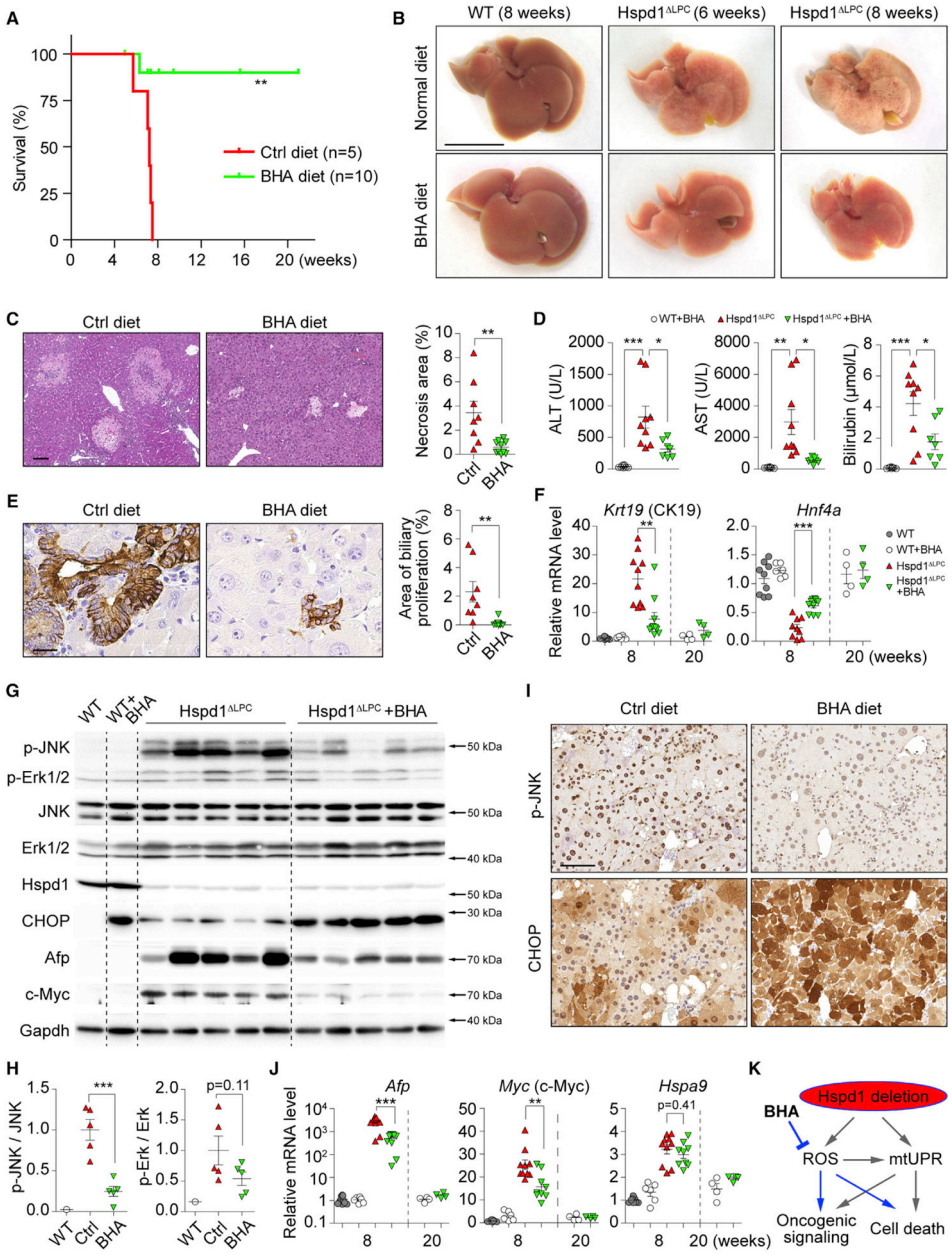

Figure 3. Anti-oxidants Attenuate ROS Accumulation and Premalignant Cholangiocellular Lesions in Hspd1$^{\Delta LPC}$ Mice

(A) Survival plots for Hspd1$^{\Delta LPC}$ mice on normal or BHA diet.

(B) Macroscopy of the liver of 6- and 8-week-old Hspd1$^{\Delta LPC}$ or 8-week-old WT mice on normal or BHA diet. Scale bar, 1 cm.

(C) H&E of the liver of 8-week-old Hspd1$^{\Delta LPC}$ mice on normal versus BHA diet and quantification of necrotic areas. Scale bar, 100 μm.

(D) Serum ALT, AST, and bilirubin in 8-week-old Hspd1$^{\Delta LPC}$ mice on normal and BHA diet.

(E) A6 IHC in 8-week-old normal versus BHA diet Hspd1$^{\Delta LPC}$ livers and quantification of cholangiocellular overgrowth. Scale bar, 20 μm.

(F) qRT-PCR of livers from 8- and 20-week-old normal versus BHA diet Hspd1$^{\Delta LPC}$ mice for *CK19* and *Hnf4a*.

(G and H) Western blot of liver lysates from 8-week-old normal versus BHA diet Hspd1$^{\Delta LPC}$ mice (G) and quantifications the p-JNK to total JNK and the p-Erk1/2 to total Erk1/2 ratio (H).

(I) IHC for p-JNK and CHOP in consecutive liver sections from normal versus BHA diet 8-week-old Hspd1$^{\Delta LPC}$ mice. Scale bar, 50 μm.

(J) qRT-PCR of livers from 8- and 20-week-old normal versus BHA diet Hspd1$^{\Delta LPC}$ mice for genes indicated.

(K) A schematic depicting the action of BHA in Hspd1$^{\Delta LPC}$ mice.

Data are represented as the mean ± SEM. *p < 0.05, **p < 0.01, ***p < 0.001. ns, not significant. See also Figure S4.

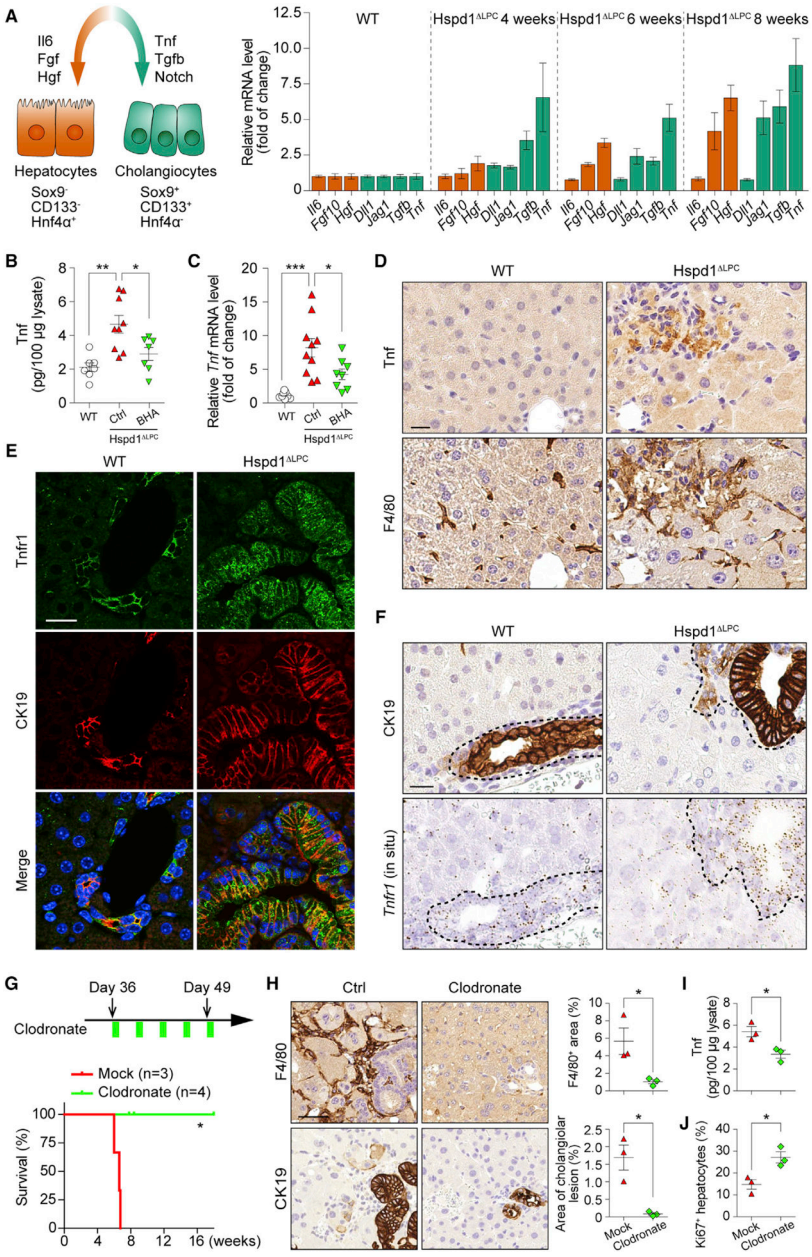

Figure 4. Kupffer Cells Promote Cholangiocellular Tumorigenesis

(A) Left: schematic of key signals regulating hepato- or cholangiocellular proliferation. Right: qRT-PCR of Hspd1$^{\Delta LPC}$ livers at different ages for the expression of key ligands.

(B and C) Tnf ELISA (B) and qRT-PCR (C) of WT and normal versus BHA diet 8-week-old Hspd1$^{\Delta LPC}$ livers.

(D) Tnf and F4/80 IHC in consecutive sections of 8-week-old Hspd1$^{\Delta LPC}$ and WT livers. Scale bar, 20 μm.

(E) Immunofluorescence (IF) of Tnfr1 and CK19 in 8-week-old Hspd1$^{\Delta LPC}$ and WT livers. Scale bar, 20 μm.

(F) CK19 IHC and Tnfr1 in situ hybridization in consecutive sections from 8-week-old Hspd1$^{\Delta LPC}$ and WT livers. The dashed lines indicate the border between bilary cells and hepatocytes. Scale bar, 20 μm.

(G) Upper: timeline of clodronate administration on Hspd1$^{\Delta LPC}$ mice. Lower: survival plot for Hspd1$^{\Delta LPC}$ mice treated with mock or clodronate.

(H) F4/80 and CK19 IHC in consecutive sections from 8-week-old Hspd1$^{\Delta LPC}$ livers treated with mock or clodronate. Quantification of each staining was shown in the right panels. Scale bar, 50 μm.

(I) Tnf ELISA from 8-week-old Hspd1$^{\Delta LPC}$ livers treated with mock or clodronate.

(J) Quantification of Ki67^{+} hepatocytes in Hspd1$^{\Delta LPC}$ livers treated with mock or clodronate.

Data are represented as the mean ± SEM. *p < 0.05, **p < 0.01, ***p < 0.001. ns, not significant. See also Figure S5.

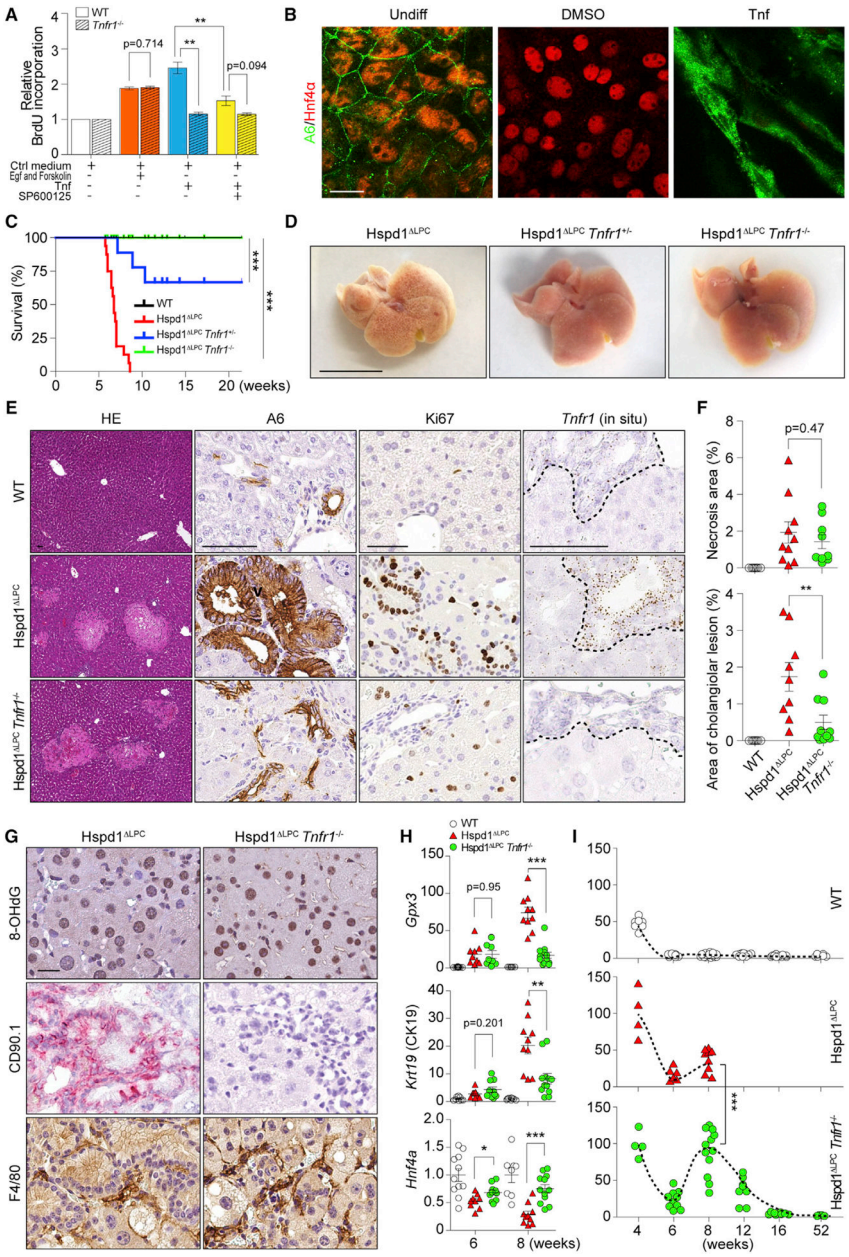

Figure 5. Tnfr1 Signaling Promotes Premalignant Cholangiocellular Lesions

(A) Cell proliferation of WT or *Tnfr1*$^{-/-}$ cholangiocytes was analyzed by bromodeoxyuridine (BrdU) incorporation.

(B) Hepatoblasts were kept in basal medium or basal medium supplemented with DMSO or Tnf. IF of A6 and Hnf4α was performed. Scale bar, 20 μm.

(C) Survival analysis for Hspd1$^{\Delta LPC}$, Hspd1$^{\Delta LPC}$ *Tnfr1*$^{+/-}$, and Hspd1$^{\Delta LPC}$ *Tnfr1*$^{-/-}$ mice.

(D) Macroscopic appearance of 8-week-old Hspd1$^{\Delta LPC}$, Hspd1$^{\Delta LPC}$ *Tnfr1*$^{+/-}$, and Hspd1$^{\Delta LPC}$ *Tnfr1*$^{-/-}$ livers. Scale bar, 1 cm.

(E and F) H&E, A6 and Ki67 IHC, and Tnfr1 in situ hybridization of 8-week-old WT, Hspd1$^{\Delta LPC}$, and Hspd1$^{\Delta LPC}$ *Tnfr1*$^{-/-}$ livers (E), as well as quantification of necrosis and

cholangiocellular overgrowth (F). The dashed lines indicate the border between bilary cells and hepatocytes. Scale bar, 50 μm.

(G) IHC of 8-week-old Hspd1$^{\Delta LPC}$ and Hspd1$^{\Delta LPC}$ *Tnfr1*$^{-/-}$ livers. Scale bar, 20 μm.

(H) qRT-PCR of 6- and 8-week-old WT, Hspd1$^{\Delta LPC}$, and Hspd1$^{\Delta LPC}$ *Tnfr1*$^{-/-}$ livers for indicated genes.

(I) Percentage of Ki67^{+} hepatocytes in WT, Hspd1$^{\Delta LPC}$, and Hspd1$^{\Delta LPC}$ *Tnfr1*$^{-/-}$ livers.

Data are represented as the mean ± SEM. *p < 0.05, **p < 0.01, ***p < 0.001. ns, not significant. See also Figure S5.

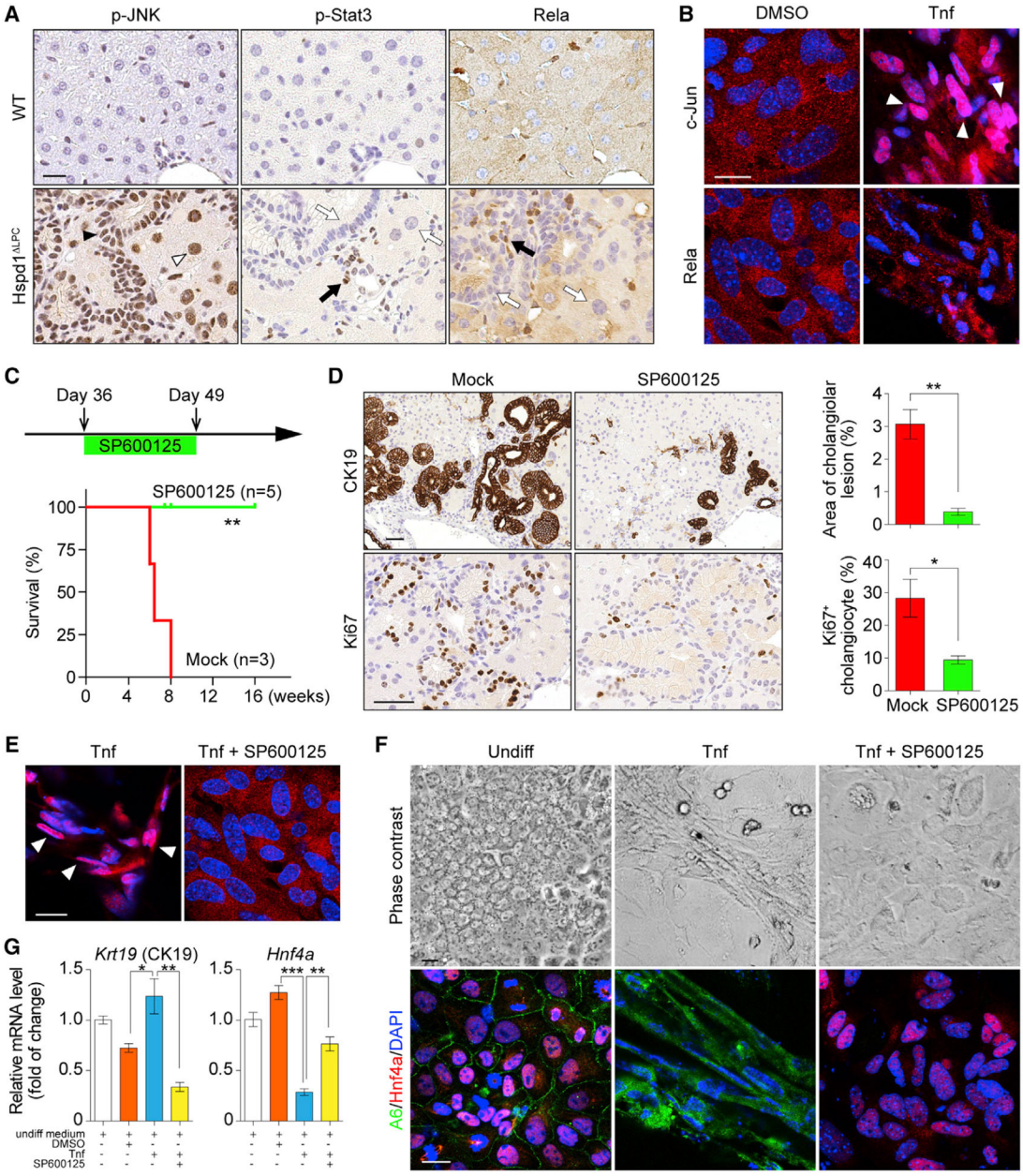

Figure 6. JNK/c-Jun Activation Is Required for Premalignant Cholangiocellular Lesions

(A) p-JNK, p-Stat3, and Rela IHC in 8-week-old WT and Hspd1$^{\Delta LPC}$ livers. The black arrowhead indicates a p-JNK^{+} cholangiocyte, the white arrowhead indicates a p-JNK^{+} hepatocyte. Black arrows indicate positive staining in non-parenchymal cells, while white arrows indicate negative staining in liver parenchymal cells. Scale bar, 20 μm.

(B) Rela and c-Jun IF in hepatoblasts cultured in basal medium supplemented with DMSO or Tnf. White arrowheads indicate c-Jun nuclear staining. Scale bar, 20 μm.

(C) Timeline of SP600125 administration on Hspd1$^{\Delta LPC}$ mice and survival of Hspd1$^{\Delta LPC}$ mice not treated (mock) or treated with SP600125.

(D) CK19 and Ki67 IHC in 8-week-old Hspd1$^{\Delta LPC}$ livers treated with mock or SP600125, and quantification of cholangiolar cancerous lesion areas and Ki67^{+} cholangiocytes relative to total cholangiocytes. Scale bar, 50 μm.

(E) c-Jun IF in hepatoblasts cultured in Tnf-containing medium with or without SP600125. White arrowheads indicate the c-Jun nuclear staining. Scale bar, 20 μm.

(F and G) Phase contrast and A6 and Hnf4α IF images (F) and qRT-PCR (G) of hepatoblasts in basal or Tnf-containing medium with or without SP600125. Scale bar, 20 μm.

Data are represented as the mean ± SEM. *$p < 0.05$, **$p < 0.01$, ***$p < 0.001$. ns, not significant. See also Figure S6.

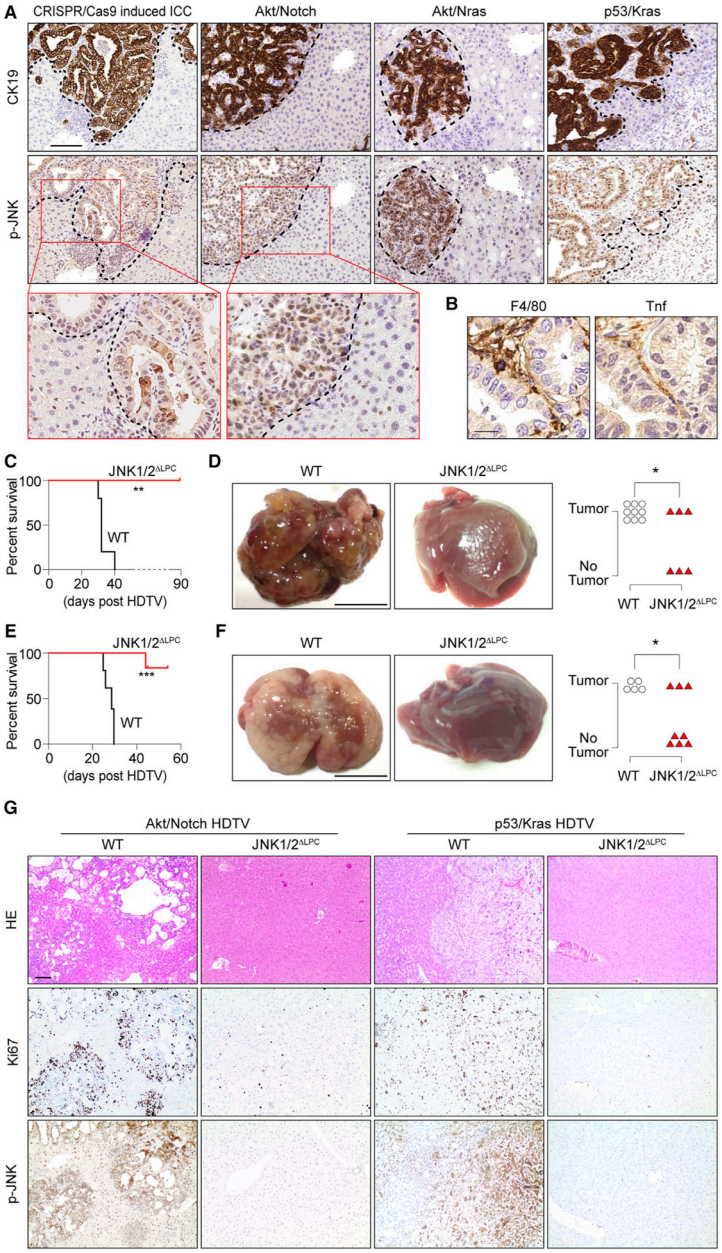

Figure 7. Kupffer Cell-Derived Tnf/JNK Axis Is Activated in Different ICC Models

(A) IHC of CK19 and p-JNK in liver sections from four ICC models as indicated. The dashed lines indicate the border between ICC and the surrounding liver tissues. Scale bar, 100 μm.

(B) F4/80 and Tnf IHC in consecutive sections from CRISPR/cas9-mediated multiplex mutagenesis livers. Scale bar, 20 μm.

(C–F) Survival plot (C and E) and representative macroscopic view of ICC and quantification of tumor incidence (D and F) for JNK1/2$^{\Delta LPC}$ and control C57BL/6 mice in HDTV-Akt/Notch-induced (C and D) or HDTV-p53/Kras-induced (E and F) ICC model. Scale bar, 1 cm.

(G) H&E and IHC staining of Ki67 and p-JNK in livers as indicated in (C and E). Scale bar, 100 μm.

*p < 0.05, **p < 0.01, ***p < 0.001. ns, not significant. See also Figure S7.

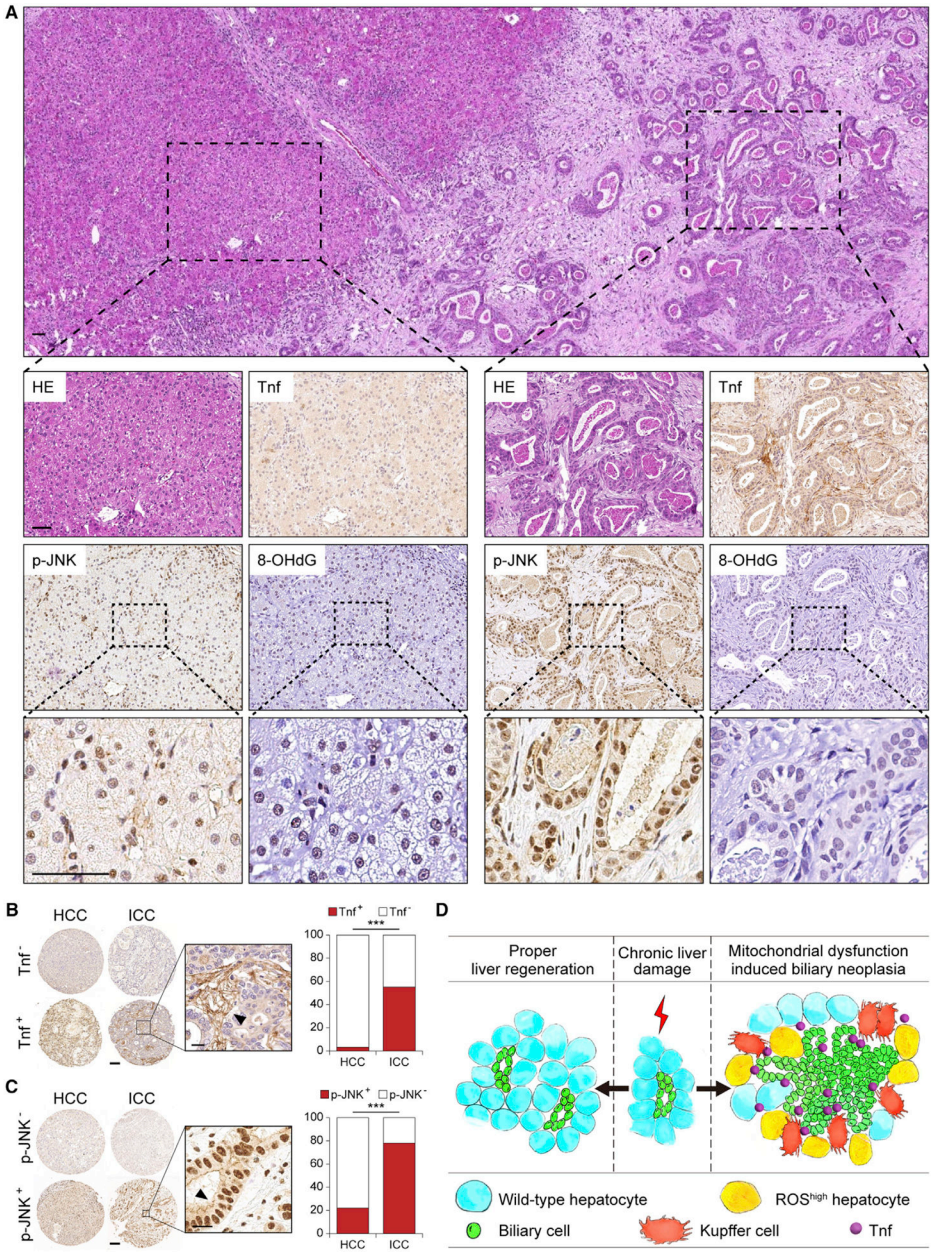

Figure 8. Tnf and p-JKN Are Strongly Increased in ICC Patient Specimens

(A) H&E and IHC staining of Tnf, p-JNK, and 8-OHdG in a representative human ICC sample. Scale bar, 50 μm.

(B and C) Representative IHC images and quantification of Tnf (B) and p-JNK (C) in human ICC and HCC. Arrowheads indicate positive staining. Scale bars, 100 μm (left), 20 μm (right).

(D) Model depicting a non-cell-autonomous mechanism of hepatocyte mitochondrial dysfunction in regulating cholangiocellular tumorigenesis.

***$p < 0.001$. ns, not significant. See also Figure S8.

KEY RESOURCES TABLE

REAGENT or RESOURCE	SOURCE	IDENTIFIER
Antibodies		
Goat anti-Hspd1	Santa Cruz	Cat# sc-1052; RRID: AB_631683
Goat anti-GP73	Santa Cruz	sc-48011; RRID: AB_2113325
Rabbit anti-c-Jun	Abcam	Cat# ab31367; RRID: AB_731606
p-c-Jun	Cell Signaling	Cat# 9164L; RRID: AB_330893
Rabbit anti-p-JNK	Abcam	Cat# ab131499; RRID: AB_11157976
Rabbit anti-JNK	Cell Signaling	Cat# 9252; RRID: AB_2250373
Rabbit anti-p-Erk1/2	Cell Signaling	Cat# 4370; RRID: AB_2315112
Erk1/2	Cell Signaling	Cat# 9107; RRID: AB_2235073
Rabbit anti-CHOP	Cell Signaling	Cat# 5554S; RRID: AB_10694399
Rabbit anti-p-p38 MAPK	Cell Signaling	Cat# 4511; RRID: AB_2139682
Rabbit anti-p38 MAPK	Cell Signaling	Cat# 9212; RRID: AB_330713
Rabbit anti-p-Akt	Cell Signaling	Cat# 4060; RRID: AB_2315049
Rabbit anti-Akt	Cell Signaling	Cat# 2938; RRID: AB_915788
Gapdh	Cell Signaling	Cat# 2118; RRID: AB_561053
Rabbit anti-Pcna	Santa Cruz	Cat# sc-7907; RRID: AB_2160375
HRP-anti rabbit IgG	Jackson	Cat# 111-055-045; RRID: AB_2337950
HRP-anti mouse IgG	Jackson	Cat# 115-035-003; RRID: AB_10015289
HRP-anti Goat	Dako	Cat# P0449; RRID: AB_2617143
Mouse anti-8-ohdg	Abcam	Cat# ab48508; RRID: AB_867461
Goat anti-Afp	R&D	Cat# AF5369; RRID: AB_2258018
Rabbit anti-Collagen Type IV	Cedarlane	Cat# CL50451AP; RRID: AB_10059811
Rabbit anti-cleaved Caspase-3	Cell Signaling	Cat# 9661; RRID: AB_2341188
Rabbit anti-Cytokeratin	Dako	Cat# Z0622; RRID: AB_2650434
Rat anti-F4/80	BioLegend	Cat# 123105; RRID: AB_893499
Rabbit anti-Glutamine Synthetase	Abcam	Cat# ab16802; RRID: AB_302521
Rabbit anti-Ki67	NeoMarkers	Cat# RM-9106-S0; RRID: AB_2341197
Rat anti-Ly6G	BD	Cat# 551459; RRID: AB_394206
Rabbit anti-Rela	NeoMarkers	Cat# RB-1638-P0; RRID: AB_59726
Rabbit anti-Tnf	Abcam	Cat# ab6671; RRID: AB_305641
Rabbit anti-Tnfr1	Abcam	Cat# ab19139; RRID: AB_2204128
Rabbit anti-c-Myc	Abcam	Cat# ab32072; RRID: AB_731658
Rat anti-CK19	Developmental Studies Hybridoma Bank	Cat# TROMA-III; RRID: AB_2133570
Bacterial and Virus Strains		
AAV8-Cre	VectorBiolabs	Cat#7060
Biological Samples		
Liver tissues from mice after bile duct ligation	Jors et al., 2015	N/A
Liver tissues from mice fed with CDE	Jors et al., 2015	N/A
Liver tissues from mice fed with DDC	Jors et al., 2015	N/A

REAGENT or RESOURCE	SOURCE	IDENTIFIER
Liver tissues from CRISPR/Cas9 mulitplex mutagenesis model	Weber et al., 2015	N/A
Chemicals, Peptides, and Recombinant Proteins		
SP600125	Abcam	CAS: 129-56-6
JNK-IN-8	Merck	CAS: 1410880-22-6
JNK6o	Bio-techne	CAS: 894804-07-0
S3I-201	Biovision	CAS: 501919-59-1
LY-294002	Sigma	CAS: 934389-88-5
Isoliquiritigenin	Sigma	CAS: 961-29-5
TPCA-1	Sigma	CAS: 507475-17-4
NBP2–29328	Novus Biologicals	Cat#NBP2–29328
Critical Commercial Assays		
Mouse Genome CGH Oligo Microarrays	Agilent	Cat#4839A
REPLI-g Whole Genome Amplification Kit	Qiagen	Cat#150025
TNF Quantikine-Elisa-Kit	R&D	Cat#SMAT00B
Mouse Il6 Elisa kit	RayBiotech	Cat#ELM-IL6
RNAscope 2.0 in situ hybridization kit	Advanced Cell Diagnostics	Cat#310033
Deposited Data		
aCGH data	This paper	The accession number for the aCGH data reported in this paper is arrayexpress: E-MTAB-4624
Intrahepatic cholangiocarcinomas data set in TCGA	TCGA	http://cancergenome.nih.gov/
Experimental Models: Cell Lines		
HuCCT-1	Roland Rad	Cellbankaustralia, JCRB0425
ETK-1	Roland Rad	N/A
HepG2	ATCC	HB-8065
Huh7	Ulrike Protzer	N/A
HepRG	Ulrike Protzer	N/A
mICC	Roland Rad	N/A
Experimental Models: Organisms/Strains		
Hspd1$^{flox/flox}$	Taconic-Artemis; Dirk Haller (Berger et al., 2016)	N/A
R26R-Confetti	Jackson	JAX: 013731
Tnfr1$^{-/-}$	Jackson	JAX: 003242
Alb-Cre	Jackson	JAX: 003574
JNK1/2$^{flox/flox}$	Roger Davis	N/A
Oligonucleotides		
qRT-PCR primers	This paper	Please see Table S1.
Recombinant DNA		
pT3 EF1a-KrasG12D-IRES-GFP	Darjus F. Tschaharganeh	N/A
pT3 EF1a-NICD-IRES-cherry	Darjus F. Tschaharganeh	N/A
pT3 EF1a-myrAKT	Xin Chen (Fan et al., 2012)	N/A
pX330 sgp53	Darjus T.	N/A

REAGENT or RESOURCE	SOURCE	IDENTIFIER
Software and Algorithms		
Agilent Technologies' Feature Extraction (version 10.7.3.1)	Agilent	http://www.agilent.com
RCircos		http://bioconductor.org
CGHcall		http://bioconductor.org
CGHregions		http://bioconductor.org